JCB Journal of Cell Biology

ARTICLE

Cell and tissue morphology determine actin-dependent nuclear migration mechanisms in neuroepithelia

Iskra Yanakieva[1], Anna Erzberger[1,2], Marija Matejčić[1], Carl D. Modes[1,3], and Caren Norden[1]

Correct nuclear position is crucial for cellular function and tissue development. Depending on cell context, however, the cytoskeletal elements responsible for nuclear positioning vary. While these cytoskeletal mechanisms have been intensely studied in single cells, how nuclear positioning is linked to tissue morphology is less clear. Here, we compare apical nuclear positioning in zebrafish neuroepithelia. We find that kinetics and actin-dependent mechanisms of nuclear positioning vary in tissues of different morphology. In straight neuroepithelia, nuclear positioning is controlled by Rho-ROCK–dependent myosin contractility. In contrast, in basally constricted neuroepithelia, a novel formin-dependent pushing mechanism is found for which we propose a proof-of-principle force generation theory. Overall, our data suggest that correct nuclear positioning is ensured by the adaptability of the cytoskeleton to cell and tissue shape. This in turn leads to robust epithelial maturation across geometries. The conclusion that different nuclear positioning mechanisms are favored in tissues of different morphology highlights the importance of developmental context for the execution of intracellular processes.

Introduction

Nuclei can be positioned differently in cells depending on cell type, cell cycle phase, migratory state, and differentiation stage (Gundersen and Worman, 2013). Nuclear positioning is a prerequisite for the correct execution of cellular programs including centered mitosis in fission yeast (Tran et al., 2001), differentiation of dermal cells in nematodes (Fridolfsson and Starr, 2010) and muscle cells in vertebrates (Roman and Gomes, 2018), and neural system development (Shu et al., 2004; Tsai and Gleeson, 2005; Tsai et al., 2007). Due to its importance for correct cell function and tissue development, the position of the cell nucleus needs to be tightly controlled. To ensure exact positioning within cells, nuclei are actively transported by cytoskeletal elements, and both actin (Gomes et al., 2005; Luxton et al., 2010) and microtubules (Reinsch and Gönczy, 1998; Tran et al., 2001; Fridolfsson and Starr, 2010) can exert pulling or pushing forces on nuclei using a variety of mechanisms. Interestingly, even within a single cell type, for example fibroblasts, the mechanisms of nuclear transport can differ depending on extracellular context (Levy and Holzbaur, 2008; Petrie et al., 2014; Wu et al., 2014). This striking variety of mechanisms not only underlines the importance of nuclear position regulation, but also illustrates the different means by which the cytoskeleton adapts to fulfill a precise task.

Diverse mechanisms of nuclear positioning have been studied extensively in cultured cells and the *Caenorhabditis elegans* zygote (Reinsch and Gönczy, 1998). However, how nuclear positioning is achieved in more complex settings, such as tissues within developing organisms, is not similarly well explored. In developing epithelia, for example, complex shape changes occur at the single cell level and at the tissue scale. To date, it is not known how robust nuclear positioning is maintained across such varying cell and tissue geometries.

Here, we address this question in pseudostratified neuroepithelia of the developing zebrafish. Pseudostratified neuroepithelia give rise to the nervous system, and correct nuclear positioning is crucial for their maturation. Nuclei in pseudostratified neuroepithelia are densely packed and occupy different apicobasal positions in interphase (Sauer, 1935; Lee and Norden, 2013) when nuclear movements are stochastic (Norden et al., 2009; Kosodo et al., 2011; Leung et al., 2011). Preceding mitosis, however, nuclei are actively moved to the apical surface (Norden et al., 2009; Kosodo et al., 2011; Leung et al., 2011; Fig. 1 A). If nuclei fail to position apically, divisions occur at basal locations,

[1]Max Planck Institute of Molecular Cell Biology and Genetics, Dresden, Germany; [2]Max Planck Institute for the Physics of Complex Systems, Dresden, Germany; [3]Max Planck Center for Systems Biology, Dresden, Germany.

Correspondence to Caren Norden: norden@mpi-cbg.de

A preprint of this paper was posted in *bioRxiv* on June 4, 2019.

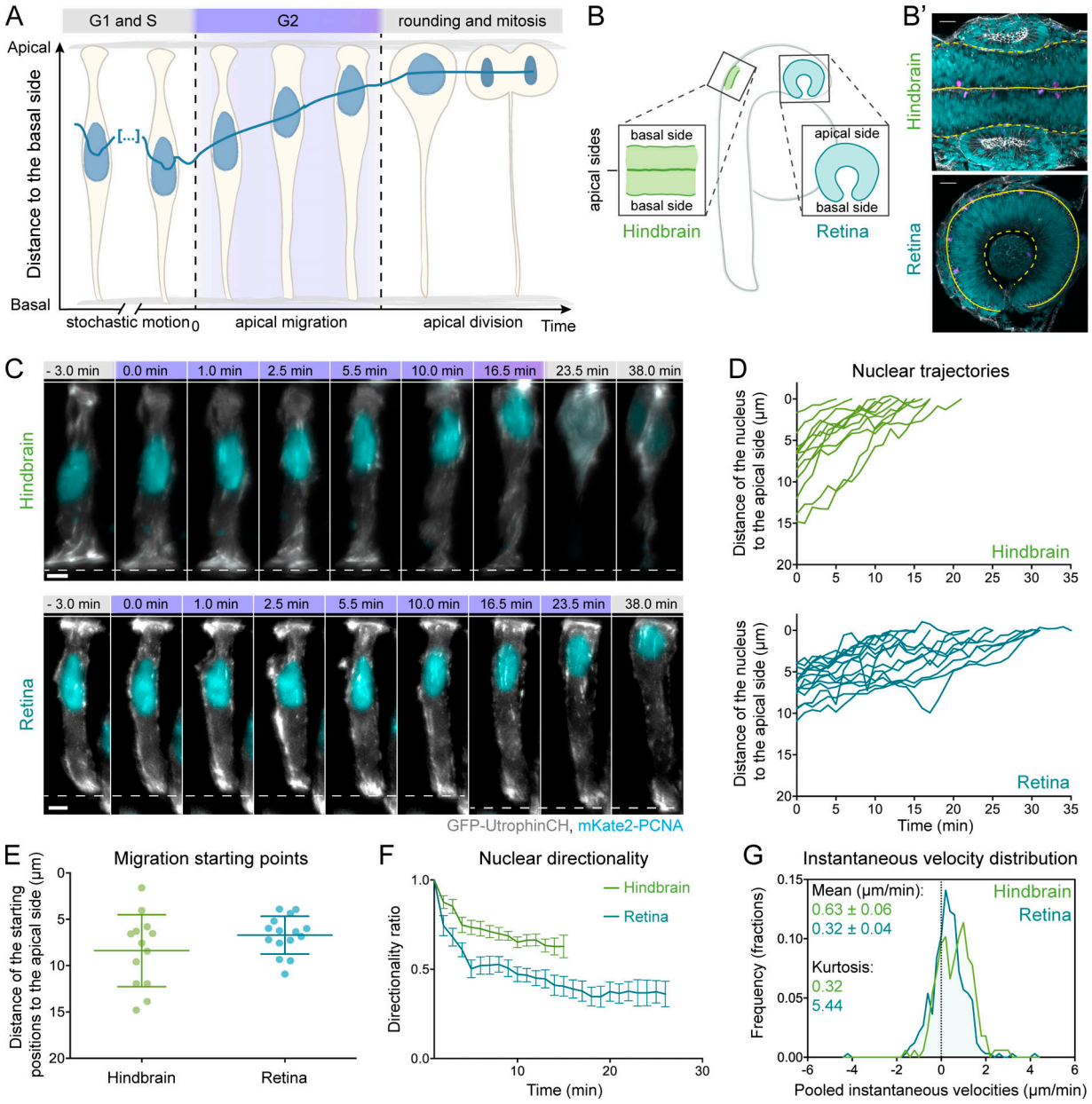

Figure 1. **Apical nuclear migration in the hindbrain is faster and more directed than in the retina. (A)** Neuroepithelial nuclei move stochastically in G1 and S and occupy diverse apicobasal positions. In G2 (highlighted in purple in the schematic and all montages), nuclei migrate to the apical side where cells divide. **(B)** Schematic of hindbrain and retinal neuroepithelia in the zebrafish embryo. Hindbrain is shown in green and retina in blue in all figures. **(B')** Morphology of hindbrain at 18 hpf and retina at 24 hpf. Nuclear staining: DAPI (cyan); actin staining: phalloidin (gray); mitotic cells: pH3 (magenta). Solid lines mark the apical and dashed lines mark the basal tissue surface in all figures. **(C)** Example of apical nuclear migration in maximum projection of hindbrain and retinal cells, imaged with LSFM (Video 1). Staining: mKate2-PCNA labels nuclei (cyan), GFP-UtrophinCH labels actin (gray). **(D)** Apical migration trajectories. Start: 0 min = entry in G2. Finish: onset of cell rounding (nuclear position at cell rounding = 0 µm from the apical side). **(E)** Starting positions of hindbrain and retinal nuclei shown as mean ± SD. Variances comparison: P = 0.0485, Levene's test. **(F)** Directionality ratios shown as mean of all tracks; error bars represent SD. Hindbrain = 0.63 ± 0.06, Retina = 0.36 ± 0.07. **(G)** Pooled instantaneous velocity distributions in hindbrain and retina. P < 0.0001, Mann-Whitney test. Scale bars: 20 µm (B'), 5 µm (C).

and these basally dividing cells perturb epithelial integrity and maturation (Strzyz et al., 2015). Interestingly, the cytoskeletal elements responsible for this crucial apical nuclear positioning differ depending on epithelium (Lee and Norden, 2013; Strzyz et al., 2016; Norden, 2017). In the extremely elongated cells of the rodent neocortex, movements are microtubule-dependent (Bertipaglia et al., 2018), and the mechanisms have been extensively studied (Shu et al., 2004; Tsai et al., 2010; Hu et al., 2013). In contrast, in shorter neuroepithelia, nuclear positioning is driven by the actin cytoskeleton (Strzyz et al., 2016). However, the mechanisms by which actin generates the forces required for apical nuclear movement are still not fully understood. Rho-associated protein kinase (ROCK) has been implicated in apical nuclear migration (Meyer et al., 2011) in

the *Drosophila melanogaster* wing disc, but it is unclear whether this mechanism is conserved in other pseudostratified epithelia. Indications that nuclear positioning mechanisms might vary have come from a study of zebrafish retina and hindbrain neuroepithelia (Leung et al., 2011). However, how mechanisms differ and whether these differences are influenced by the tissue context remains elusive. Here, we investigate apical nuclear migration in zebrafish hindbrain and retinal neuroepithelia (Fig. 1, B and B'). We reveal differences in nuclear kinetics between these tissues and show that these differences result from different actin-dependent mechanisms: in the hindbrain, the Rho-ROCK pathway is involved in apical nuclear migration, while in the retina, nuclear movements are driven by a formin-dependent pushing mechanism. We demonstrate that these mechanistic differences are conserved in other tissues, morphologically comparable to hindbrain and retina, and that migration modes can change when cell and tissue shape changes are induced.

Results

Apical migration of retinal and hindbrain nuclei occurs with different kinetics

To understand the kinetic differences between apical nuclear migration in hindbrain and retinal neuroepithelia (Leung et al., 2011; Fig. 1 B), we tracked nuclear movements in both tissues using light sheet fluorescent microcopy (LSFM) at sub-minute resolution (Icha et al., 2017; Fig. 1 C). The G2 phase of the cell cycle, during which active nuclear migration occurs, was identified using a proliferating cell nuclear antigen (PCNA) marker (Leung et al., 2011; Strzyz et al., 2015; Fig. 1 C and Video 1). Nuclear trajectory analysis (Fig. 1 D) revealed that nuclei in the retina generally start G2 movements relatively close to the apical surface (Fig. 1 E), while the variance of starting points was greater in the hindbrain (Fig. 1 E and Table 1). Nevertheless, hindbrain nuclei migrated for shorter times than retinal nuclei (Table 1), indicating more directed movements. Quantitative analysis of apical nuclear movements confirmed that hindbrain nuclei indeed displayed a higher average instantaneous velocity compared with retinal nuclei (Table 1, Fig. 1 G, and Fig. S4 H). Further, directionality ratio (Fig. 1 F and Table 1) and mean squared displacement analysis (Fig. S1 A) revealed a higher directionality of hindbrain nuclei (Table 1). Characterization of instantaneous velocity distributions showed that retinal nuclei more frequently undergo negative (basal) movements than hindbrain nuclei (Fig. 1 G). Comparing the kurtosis, a measure of the contribution of infrequent extreme deviations to the tails of the distribution, confirmed that extreme deviations were more common in retina than in hindbrain (Table 1 and Fig. 1 G). Together, these data indicated that retinal nuclei move in a more saltatory manner than hindbrain nuclei.

Overall, our analysis confirms that apical nuclear movements differ between hindbrain and retina. While nuclei in the hindbrain start migrating from more variable apicobasal positions and move toward the apical surface in a directed and smooth manner, nuclei in the retinal neuroepithelium start more apically, and their movements are slower and less directed. These results made us speculate that the observed differences in the motion of hindbrain and retinal nuclei could result from different forces that move nuclei in the two tissues.

Only retinal neuroepithelial nuclei show persistent aspect ratio changes during nuclear migration

If our hypothesis that different forces propel hindbrain and retinal nuclei during apical migration was correct, we assumed that we could infer these forces from nuclear deformations during movement. Nuclear deformability is inversely related to nuclear stiffness that depends predominantly on the expression of A-type lamins (Rowat et al., 2013; Swift et al., 2013; Harada et al., 2014). Different parts of the developing mouse brain were shown to express low levels of Lamin A/C (Jung et al., 2012; Cho et al., 2019), which could suggest that in neuroepithelia, nuclei are deformable and that their shape would change under the action of forces. To assess nuclear deformability in zebrafish neuroepithelia, we compared the expression levels of Lamin A/C and Lamin B1 in retinal and hindbrain nuclear envelopes. We found that while Lamin B1 was evenly distributed at nuclear envelopes of both tissues (Fig. 2 A), Lamin A/C was absent (Fig. 2 A; Lamin A/C control staining [Fig. S2 B]), suggesting that indeed neither hindbrain nor retinal nuclei were rigid. Live imaging of nuclei expressing the nuclear envelope marker LAP2b corroborated this notion, revealing frequent deformations and dynamic indentations of nuclear envelopes (Fig. 2 B and Video 2). We analyzed these nuclear deformations for S- and G2-phase nuclei of both neuroepithelia by 3D nuclear segmentation (Fig. 2 C). In S phase, nuclei in both tissues showed elongated, ellipsoidal shapes (Fig. 2 C). However, nuclei underwent frequent periods of deformation and relaxation fluctuating around the average with comparable variances (Fig. 2 D, Fig. S1 C, and Table 1). While in G2 the aspect ratio of hindbrain nuclei fluctuated around a similar average as in S phase, retinal nuclei persistently increased their aspect ratio in G2 and became more ovoid (Fig. 2 D and Table 1).

Cross-correlation analysis showed that correlations between the dynamics of nuclear aspect ratio and instantaneous velocities in the retina were on average higher in G2 than in S phase (Fig. 2 E and Fig. S1 D). The correlation between nuclear velocity and shape changes in retinal G2 nuclei suggested that both are caused by fluctuations in the force that propels retinal nuclei apically. One possible explanation for the shortening of retinal nuclei during migration was that they were being pushed to the apical side by a force originating basally of the nucleus. To test this notion, we performed laser ablation of a circular region in the center of hindbrain and retinal S and G2 nuclei (Fig. S1 E). To identify cell cycle phase, nuclei were labeled with GFP-PCNA (Fig. S1 F). H2B-RFP was used as a chromatin marker to visualize changes in the shape of the ablated regions (Fig. S1, F and G). In S phase, the ablated regions of all retinal and hindbrain nuclei remained circular (Fig. S1 G). Similarly, no ablated region deformation was observed for G2 hindbrain nuclei. In retinal G2 nuclei, however, the ablated region frequently shortened in

Table 1. **Nuclear migration kinetics and shape change parameters that differ between hindbrain and retina**

Parameter	Hindbrain	Retina	P values
Starting positions (distance to the apical side, µm)	8.4 ± 3.9	6.7 ± 2.04	0.1266
Variance of starting positions (µm²)	15.01	4.16	0.0485
Duration of apical migration (min)	13.3 ± 4.5	21.9 ± 7.9	0.0052
Mean instantaneous velocity (µm/min)	0.63 ± 0.74	0.32 ± 0.77	<0.0001
Directionality ratio	0.63 ± 0.06	0.36 ± 0.07	–
Kurtosis of instantaneous velocity distribution	0.32	5.44	–
Normalized nuclear aspect ratio (S)	0.00 ± 0.09	0.00 ± 0.10	0.7892
Normalized nuclear aspect ratio (G2)	0.01 ± 0.16	0.17 ± 0.25	<0.0001
Variance of the normalized nuclear aspect ratio (S)	0.008	0.001	0.02199
Variance of the normalized nuclear aspect ratio (G2)	0.026	0.063	0.0001

Values shown represent mean ± SD. P values were calculated using Levene's test for the variance of starting positions of migration and variances of the normalized nuclear aspect ratio and Mann-Whitney test for starting positions of migration, duration of apical migration, instantaneous velocity, and normalized nuclear aspect ratios. –, not applicable.

apicobasal direction and in some cases showed a basal indentation (Fig. S1, G and H), in agreement with a basal force acting on nuclei.

Together, these data indicated that nuclei in the retina are subjected to pushing forces in G2, while forces are evenly distributed during migration of G2 hindbrain nuclei.

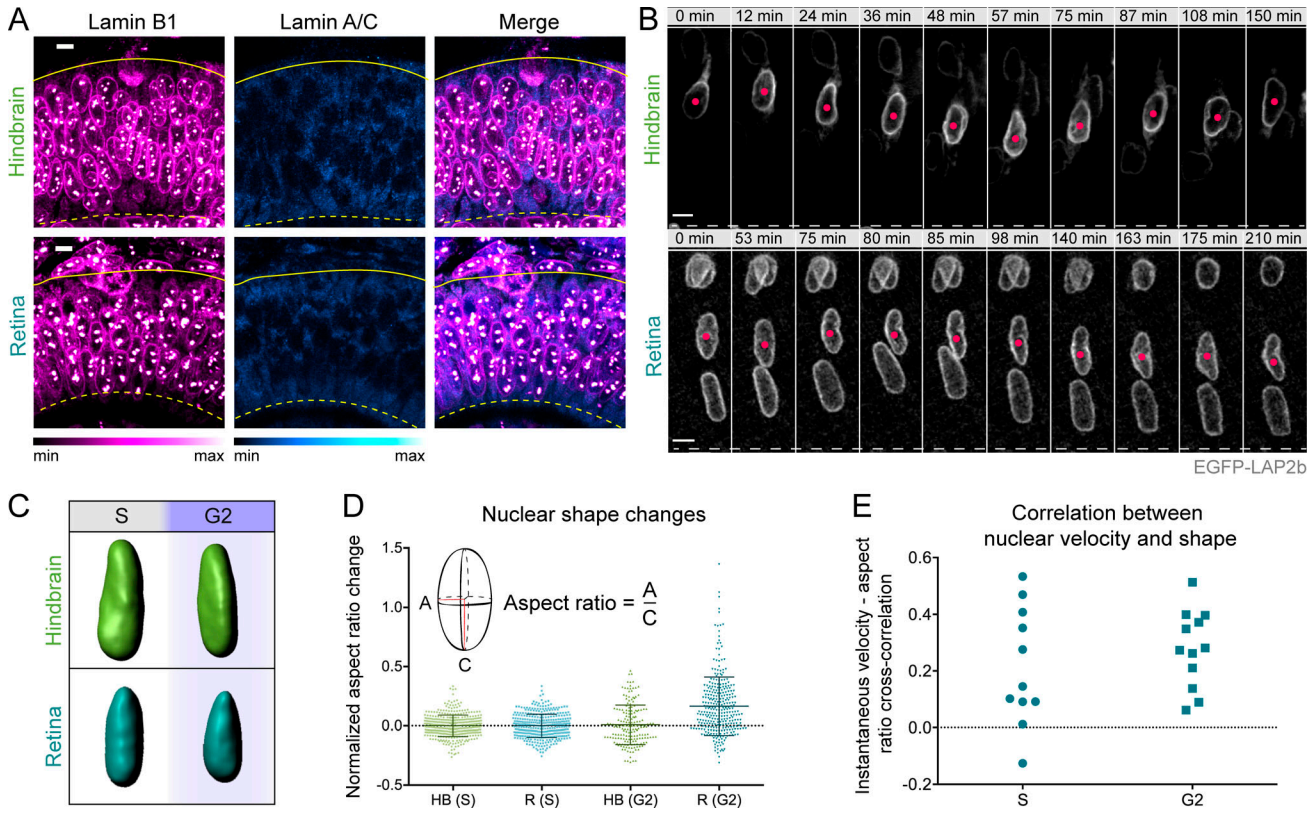

Figure 2. **Hindbrain and retinal nuclei are deformable and experience different forces during apical nuclear migration. (A)** Immunostaining of Lamin B1 and Lamin A/C in hindbrain and retinal cells (lookup tables indicate minimal and maximal signal values). **(B)** Dynamics of nuclear deformations in interphase hindbrain and retinal cells, visualized with nuclear envelope marker EGFP-LAP2b (Video 2). **(C)** 3D segmentation of hindbrain and retinal nuclei in S and G2. **(D)** Aspect ratio variability in S and G2 hindbrain (HB) and retinal (R) cells. S-phase nuclei display similar variances in nuclear aspect ratio (P = 0.7892, Levene's test, Table 1). In G2, the variance and the mean aspect ratio increase more strongly for retinal nuclei (P < 0.0001, Levene's test, and P < 0.0001, Mann-Whitney test, respectively). **(E)** Cross-correlation analysis of nuclear instantaneous velocity and aspect ratio changes in the retina shows increased average correlation in G2. Error bars: SD. Scale bars: 5 µm.

Distinct actomyosin pools are involved in nuclear movements in hindbrain and retina

To understand the different forces that drive apical nuclear migration in hindbrain and retina, we probed the cytoskeletal elements involved in their generation. In pseudostratified epithelia these forces have been shown to be generated by microtubules (Shu et al., 2004; Tsai et al., 2010; Hu et al., 2013; Strzyz et al., 2016) or actomyosin (Norden et al., 2009; Meyer et al., 2011). While it is known that in retinal neuroepithelia, apical nuclear migration is actomyosin-dependent (Norden et al., 2009; Strzyz et al., 2015), the cytoskeletal elements that move nuclei in hindbrain neuroepithelia were yet unspecified. We thus performed colcemid and blebbistatin treatment to interfere with microtubule or actomyosin activity, respectively. As shown before, blebbistatin but not colcemid treatment impaired apical nuclear movement in the retina (Norden et al., 2009; Strzyz et al., 2015; Fig. S2, A–C; and Video 3). The same was true for the hindbrain (Fig. S2, A–C; and Video 3). This means that nuclear migration is microtubule-independent and actomyosin-dependent in both neuroepithelia. The importance of the actin cytoskeleton in moving nuclei apically in both tissues was confirmed by combined interference with actin polymerization using latrunculin A and actin turnover using jasplakinolide (Fig. S2 D and Video 3).

We find that the same cytoskeletal elements drive nuclei to apical positions in retina and hindbrain, but their migration kinetics differ. We thus hypothesized that actin itself acts differently on nuclei of the two different epithelia, leading to differences in migration kinetics and nuclear deformations. To test this idea, we investigated actin localization in hindbrain and retinal cells during S and G2. In hindbrain, the actin signal was mainly localized to the cell periphery in both cell cycle phases (Fig. 3, A, B, and B'; Fig. S2 E; and Video 4). In retinal tissue, actin was also seen in the cytoplasm of S-phase cells, where the actin profile showed a high degree of variability (Fig. 3 A, Fig. S2 E, and Video 4). During retinal G2, however, actin became considerably and more persistently enriched basally to the nucleus, and the actin enrichment followed the organelle during migration (Fig. 3, A, B, and B'; and Video 4). Live imaging and analysis of myosin distribution also showed cytoplasmic enrichment basal to the nucleus in G2 retinal but not hindbrain cells (Fig. S2, F and G). Interestingly, the G2 actin "cloud" following the nucleus in retinal cells did not have persistent intensity profiles but fluctuated with a similar frequency as the nuclear instantaneous velocity and aspect ratio (Fig. 3, C and D; Fig. S2 H', H", and I; and Video 4). Cross-correlation analysis showed a higher correlation of basal actin intensity with nuclear aspect ratio and lower with instantaneous velocity (Fig. 3 E). This suggested that the basal actin enrichment is involved in the force-generation mechanism propelling retinal nuclei apically and that the same forces are responsible for the nuclear deformations that accompany retinal G2 movements.

Together, these data demonstrate that actin and myosin are the cytoskeletal elements driving apical nuclear migration in both hindbrain and retina. However, different actin pools act during apical nuclear migration of hindbrain and retinal cells, generating different forces that propel nuclei to the apical side.

Different actomyosin regulators control apical nuclear movements in hindbrain and retinal cells

To dissect if and how actomyosin is controlled differently during apical nuclear migration in the different neuroepithelial cells, we investigated its upstream regulators. One pathway that regulates both myosin activity and actin polymerization, the Rho-GTPase–ROCK pathway, was previously suggested to be involved in apical nuclear migration in the *Drosophila* wing disc (Meyer et al., 2011). We thus interfered with RhoA-GTPase or its effector ROCK, using the small molecule inhibitors Rhosin, combined with Y16 (Fig. S3 A and Video 6), and Rockout (Fig. 4 B and Video 5), respectively. Compared with controls (Fig. 4, A and A'), both treatments led to impaired apical nuclear movement in hindbrain. Some G2 nuclei never reached the apical surface, resulting in basal mitosis (Fig. 4, B, B', and D; Fig. S3 A; and Videos 5 and 6). Surprisingly, however, this was not the case in the retina. Here, nuclei moved as in controls (Fig. 4, B, B', and D; Fig. S3 A; and Videos 5 and 6). The results were confirmed by overexpression of a dominant-negative ROCK variant, DN-Rok2 (Marlow et al., 2002; Fig. 4 F and Video 7). Hence, apical migration in the hindbrain but not in the retina depends on ROCK-dependent activation of myosin.

Despite its independence of the Rho-GTPase–ROCK pathway, general myosin inhibition by blebbistatin stalls apical nuclear migration also in the retina (Norden et al., 2009). We therefore tested whether another common myosin activator, myosin light-chain kinase (MLCK), was involved in nuclear movements by interference with MLCK activity using the inhibitor ML-7 (Fig. S3 B and Video 6). This treatment had no effect on apical nuclear migration in the hindbrain but led to basally stalled G2 nuclei in the retina (Fig. S3 B). As earlier studies showed that MLCK can be involved in the formation and contractility of distinct pools of actin stress fibers (Totsukawa et al., 2000), we tested the role of different actin nucleators in the process. Using the small molecule CK-666 to inhibit the Arp2/3 complex, responsible for branched actin nucleation, had no effect on apical nuclear migration in retinal or hindbrain neuroepithelia (Fig. S3 C and Video 6). This result was confirmed by overexpression of a dominant-negative variant of the Arp2/3 activator NWASP (Icha et al., 2016a; Fig. S4, A and B; and Video 7). Another major actin nucleator protein family is the family of formins. Application of the pan-formin inhibitor SMIFH2 had no effect on nuclear migration in hindbrain (Fig. 4, C and C'; and Video 5). In contrast, nuclei in retinal tissues treated with SMIFH2 often stalled basally for hours or did not reach the apical surface at all (Fig. 4, C, C', and E; and Video 5).

As formins constitute a diverse protein family, we set out to identify the formins involved in nuclear migration in the retinal tissue. One suggestion came from a transcriptomics analysis (GEO accession number GSE124779 [Sidhaye and Norden, 2017]) that showed Fmnl3 (formin-like 3 protein) expression in the retina, which was confirmed by in situ hybridization (Fig. S4 C). Expression of GFP-tagged Fmnl3 revealed that the protein forms patches localized predominantly at the cell cortex in retinal progenitors (Fig. 4, H and H'; and Video 8). During G2 these Fmnl3 patches were enriched 5–10 µm basally of the nucleus (Fig. 4, H and H'; and Video 8), indicating that the observed actin

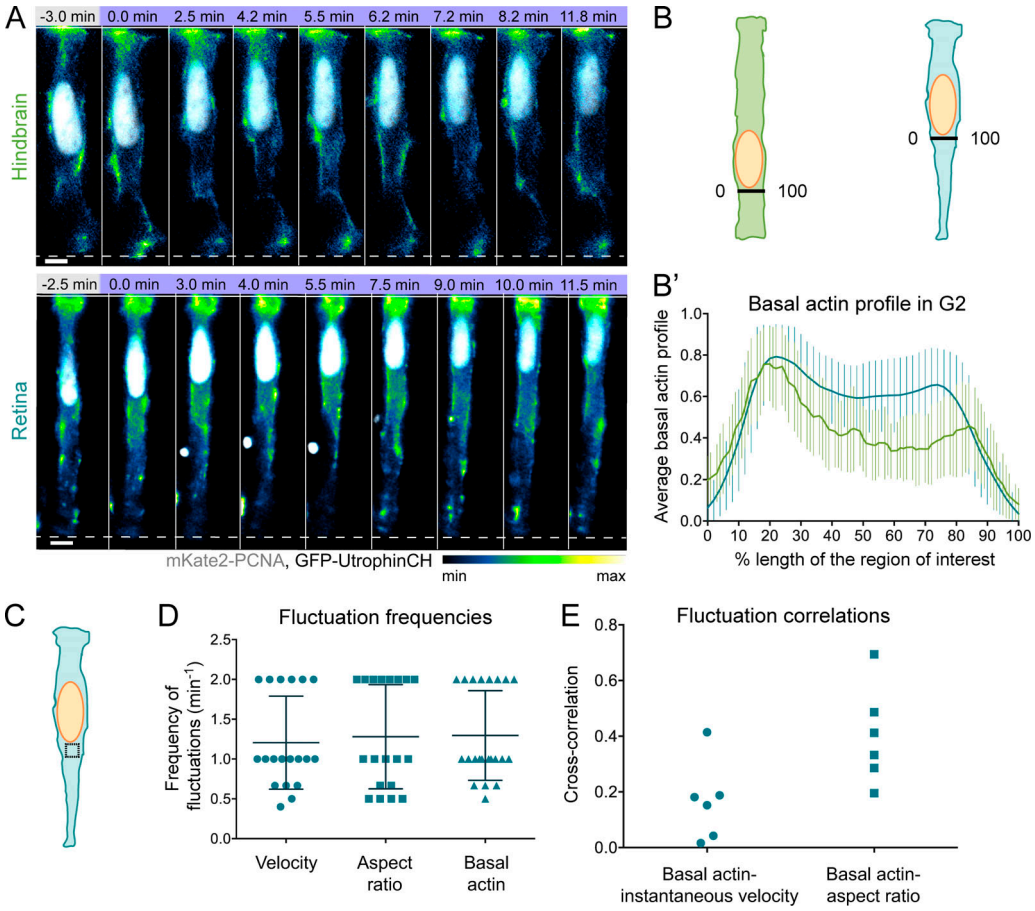

Figure 3. **Distinct actomyosin pools are involved in apical nuclear migration in hindbrain and retina. (A)** Actin distribution before and during apical migration in hindbrain and retinal cells (shown is the central z plane of a 3D stack; Video 4). mKate2-PCNA labels nuclei (gray), GFP-UtrophinCH labels actin (lookup table indicates minimal and maximal GFP-UtrophinCH signal values). Scale bar: 5 µm. **(B)** Region basal of the nucleus where GFP-UtrophinCH signal intensity was measured in the cells depicted in A. **(B')** Normalized average intensity distribution of GFP-UtrophinCH signal. The mean profile of all G2 time points is shown; error bars: SD. **(C)** Region where average GFP-UtrophinCH fluorescence intensity was measured basally to the nucleus in a z projection summing the intensities of all slices. **(D)** Pooled fluctuation frequencies of instantaneous velocity, nuclear aspect ratio, and basal actin intensity for the same retinal cell. Error bars: SD. P = 0.46 and P = 0.05 for the pairs velocity-actin and aspect ratio–actin, respectively, Mann-Whitney test. **(E)** Cross-correlation analysis between the fluctuations in basal actin and instantaneous velocity, as well as basal actin and nuclear aspect ratio.

cloud basal to retinal nuclei (Fig. 3 A) was nucleated by Fmnl3. No basal Fmnl3 patches were observed in hindbrain cells (Fig. 4 H). Specific interference with Fmnl3 activity by overexpression of a dominant-negative version, Fmnl3ΔC (Phng et al., 2015), demonstrated that indeed Fmnl3 perturbation affected apical nuclear migration in retinal but not hindbrain tissue (Fig. 4 G and Video 7).

These results show that while actin is the main driver of apical nuclear migration in both neuroepithelia, different actin regulators are at play (Fig. S3 D). In hindbrain, apical nuclear movement depends on Rho-GTPase–ROCK, while in the retina, MLCK-dependent contractility and formin-dependent actin polymerization are involved.

One possibility for a formin-dependent mechanism to generate force to propel nuclei is by the expansion of an actin network that directly pushes nuclei apically. To test if such a mechanism could fit our findings, we used our measured parameters combined with parameters taken from the literature to generate a proof-of-principle theoretical model for apically directed pushing. This working model recapitulates the observed saltatory movement of retinal nuclei and their average velocity and offers a possible explanation for the dependence of the process on formin and myosin activity (Fig. 4 I and see Discussion for model details).

Different actin-dependent mechanisms of apical nuclear migration are linked to different cell and tissue shape

We showed that hindbrain and retinal neuroepithelial cells employ distinct actomyosin-dependent force generation mechanisms to move nuclei. This is surprising taking into consideration that these tissues display a similar pseudostratified architecture and exist at similar developmental stages in the same organism. One possible explanation why nevertheless different mechanisms are used comes from a previous hypothesis that single-cell morphology as well as tissue-wide parameters like tissue shape or thickness could influence the cytoskeletal mechanisms generating the forces for apical nuclear migration (Strzyz et al., 2016). We thus tested whether cell and

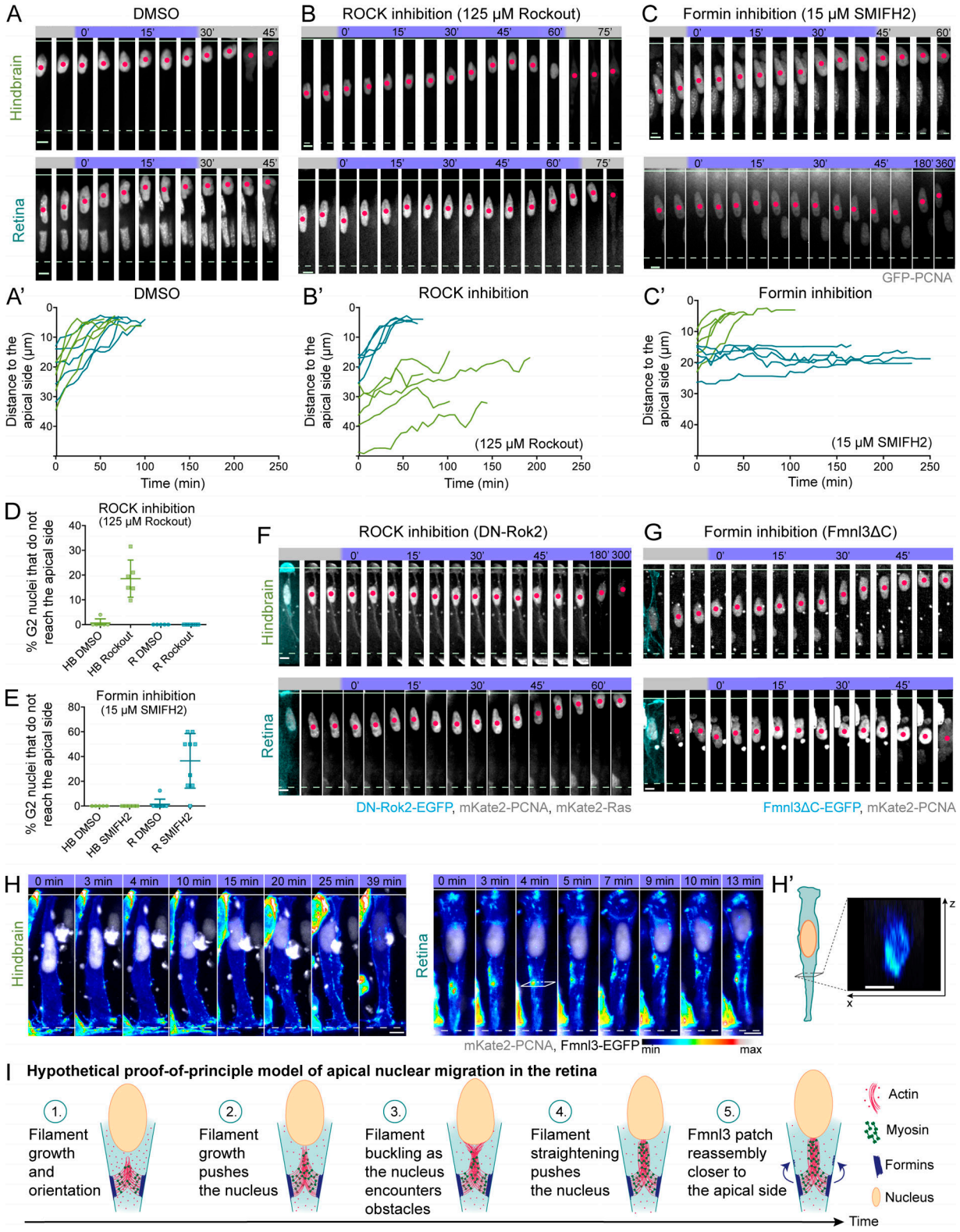

Figure 4. **Different actomyosin regulators control apical nuclear movements in hindbrain and retinal cells. (A–C)** Representative time-series of hindbrain and retinal cells treated with different actomyosin inhibitors (Video 5). **(A'–C')** Representative trajectories of treated cells. Samples were incubated in DMSO (A and A'), 125 µM Rockout (ROCK inhibitor; B and B'), or 15 µM SMIFH2 (C and C'). **(D and E)** Percentage of G2 nuclei in samples treated with Rockout (D) or SMIFH2 (E) unable to reach the apical side in hindbrain (HB) and retina (R). Error bars: SD. P = 0.0001 for Rockout-treated and P = 0.0050 for SMIFH2-treated samples, Mann-Whitney test. **(F and G)** Representative time series of hindbrain and retinal cells expressing heat shock–induced DN-Rok2-EGFP (cyan; F) and GFP-PCNA (gray) or FmnI3ΔC-EGFP (cyan; G) and mKate2-PCNA (gray; Video 8). **(H)** Representative time series of hindbrain and retinal cells expressing Fmnl3-EGFP (maximum intensity projection; lookup table indicates minimal and maximal Fmnl3-EGFP signal values) and mKate2-PCNA (gray; Video 8).

(H') Orthogonal (x-z) cross section of the retinal cell's basal process. Fmnl3-EGFP is seen enriched basally of the retinal nucleus. Scale bars: 5 µm. **(I)** Proof-of-principle theoretical model of a pushing mechanism that could drive apical nuclear migration in the retina (for details, see Discussion and Online supplemental text).

tissue morphology could influence the force generation mechanism observed in retinal versus hindbrain neuroepithelia. To this end, we analyzed tissue thickness, cell shape (Fig. S4, D and E; and Table 2), and tissue-wide actomyosin distribution in both neuroepithelia (Fig. 5, A, A', and B). While tissue thickness was similar in retina and hindbrain (Fig. S4 D and Table 2), cell shape differed. Hindbrain cells were cylindrical with comparable apical and basal cell surface area (Fig. S4 E and Table 2), whereas retinal cells had a more conical shape with the cells' apical surface areas greater than the basal surface areas (Fig. S4 E and Table 2). Cell shape differences were also reflected by different neuroepithelial geometry: a straight epithelium in hindbrain and a basally constricted epithelium in the retina (Fig. 1, B and B'). To understand the possible connections between tissue shape and force generation mechanisms, we further asked whether tissue-wide actin and myosin distribution could be different in the two neuroepithelia. We found that the tissue-wide distribution of actin, myosin, and nuclei along the apicobasal axis differed. In hindbrain, actin and myosin were evenly distributed along the lateral cell borders, with peak intensities at apical and basal surfaces and nuclei dispersed all along the apicobasal axis (Fig. 5, A' and B). In retinal tissue, however, a basal bias of actin and myosin existed (Sidhaye and Norden, 2017; Matejčić et al., 2018; Fig. 5, A' and B) that likely limited the access of nuclei to the basal portion of the tissue and thus led to the formation of a nuclear exclusion zone (Fig. 5, A' and B; Matejčić et al., 2018).

To test whether the observed differences in tissue architecture and distribution of the actomyosin cytoskeleton influence apical nuclear movements, we investigated the process in other straight or basally constricted zebrafish neuroepithelia at the midbrain-hindbrain boundary (MHB). The MHB is basally constricted at a point, termed MHBC (Gutzman et al., 2008), while its neighboring regions (referred to as MHBS) are straight (Fig. 5, C and D). Like retina and hindbrain, MHBS and MHBC had comparable thickness (Fig. S4 D and Table 2) but differed in cell shape (Fig. S4 E and Table 2). In concert with our findings in retina and hindbrain, actomyosin and nuclear distribution in the basally constricted MHBC matched findings in retinal tissue, while MHBS regions were comparable to hindbrain (Fig. 5, D and E; and Table 2).

Concluding that MHBS displayed similar cell and tissue morphology as hindbrain tissue while MHBC was similar to the retina, we tested whether nuclear migration characteristics reflected these architectural similarities. Indeed, nuclear trajectories in the two basally constricted neuroepithelia (MHBC and retina) showed striking resemblance, as did the trajectories in the two straight neuroepithelia (MHBS and hindbrain; Fig. 5 F). The duration of apical nuclear migration in the straight tissues was shorter than in the two basally constricted tissues (Fig. S4 F and Table 2). Hence, G2 nuclei in MHBS moved faster than those in MHBC, and mean instantaneous velocities between MHBS and hindbrain matched, as did velocities between MHBC and retina (Fig. S4 G and Table 2). Furthermore, nuclear movements in MHBS showed a higher directionality ratio than in MHBC (Fig. 5 G and Table 2), and MHBC nuclei, like retinal nuclei, changed their aspect ratio during G2, while the nuclear aspect ratio changed significantly less in MHBS cells (Fig. 5 H and Table 2). Further, live imaging of G2 actin showed a cloud of actin accumulation following the nucleus in MHBC, similarly to actin in retinal cells (Fig. 5 I and Video 9), while in MHBS cells, actin remained cortical during apical movement, similar to actin in hindbrain (Fig. 5 I and Video 9). To investigate whether the

Table 2. **Tissue architecture, nuclear migration kinetics, and shape change parameters that differ between straight and curved neuroepithelial tissues**

Parameter	Straight tissues		Curved tissues		P values			
	Hindbrain	MHBS	Retina	MHBC	HB-MHBS	R-MHBC	HB-R	MHBS-MHBC
Cell length (µm)	45.32 ± 4.19	38.27 ± 4.6	46.13 ± 5.13	41.54 ± 4.6	0.1017	0.0053	0.5780	0.0872
Apical-to-basal footprint ratio	1.25 ± 0.47	1.46 ± 0.76	2.32 ± 0.76	2.32 ± 1.28	0.1312	0.2617	<0.0001	<0.0001
Duration of apical migration (min)	13.3 ± 4.5	11.3 ± 2.5	21.9 ± 7.9	17.8 ± 6.6	0.3540	0.2457	0.0052	0.0326
Mean instantaneous velocity (µm/min)	0.63 ± 0.74	0.66 ± 0.68	0.32 ± 0.77	0.36 ± 0.52	0.9423	0.7831	<0.0001	0.0038
Directionality ratio	0.63 ± 0.06	0.67 ± 0.01	0.36 ± 0.07	0.53 ± 0.01	–	–	–	–
Normalized nuclear aspect ratio (G2)	0.01 ± 0.16	0.12 ± 0.13	0.17 ± 0.25	0.24 ± 0.31	<0.0001	0.0324	0.0001	0.0221
Variance of the normalized nuclear aspect ratio (G2)	0.026	0.017	0.063	0.096	0.0402	0.0007	0.0001	<0.0001

Values shown represent mean ± SD. All P values were calculated using Mann-Whitney test, except for the variances of the normalized nuclear aspect ratio, for which Levene's test was used. –, not applicable.

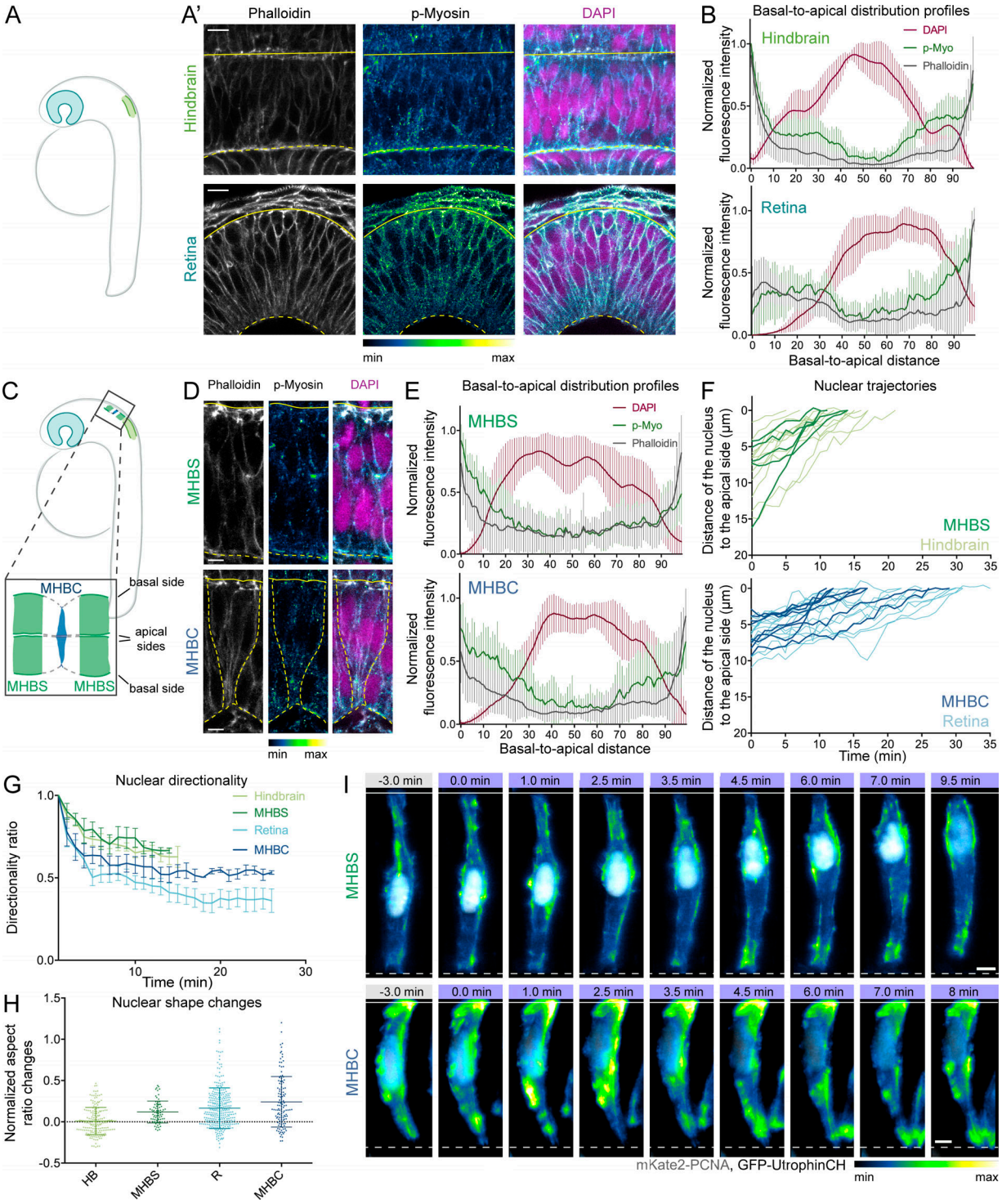

Figure 5. **Different actin-dependent mechanisms of apical nuclear migration are linked to cell and tissue shape. (A)** Schematic of the position and morphology of hindbrain and retinal neuroepithelia. **(A')** Distribution of phalloidin (actin, gray), p-Myo (active [phosphorylated] myosin; lookup table indicates minimal and maximal signal values), and DAPI (nuclei, magenta) in hindbrain and retinal neuroepithelia. **(B)** Normalized average intensity distributions of phalloidin, p-Myo, and DAPI along the apicobasal axis of hindbrain and retinal neuroepithelium. The mean of all samples is shown; error bars: SD. **(C)** Schematic of the position and morphology of MHBS and MHBC neuroepithelia. MHBS: dark green; MHBC: dark blue. **(D)** Distribution of phalloidin (actin, gray), p-Myo (lookup table indicates minimal and maximal signal values), and DAPI (nuclei, magenta) in MHBS and MHBC neuroepithelia. **(E)** Normalized average intensity distributions of phalloidin, p-Myo, and DAPI signal in MHBC and MHBS. The mean of all samples is shown; error bars: SD. **(F)** MHBS and MHBC nuclear trajectories compared with hindbrain and retinal trajectories. Hindbrain and retinal trajectories correspond to Fig. 1 D. **(G)** Directionality ratios of MHBS and MHBC nuclei. The mean of all tracks is shown, with hindbrain and retinal data corresponding to Fig. 1 F. Error bars: SD. Final directionality ratios: MHBS = 0.67 ± 0.01, MHBC = 0.53 ± 0.01. **(H)** Average nuclear aspect ratio change in MHBS and MHBC with the onset of G2 ($P = 0.0221$, Mann-Whitney test). Hindbrain (HB) and retinal (R) aspect ratio changes correspond to Fig. 2 D. Error bars: SD. **(I)** Actin distribution before and during apical migration in MHBS and MHBC cells (shown is the maximum projection of the 3D stack's central five z planes; Video 9). mKate2-PCNA labels nuclei (gray), and GFP-UtrophinCH labels actin (lookup table indicates minimal and maximal GFP-UtrophinCH signal values). Scale bars: 10 µm (A), 5 µm (D and I).

pathways responsible for apical nuclear migration were also conserved between tissues of similar morphology, we blocked Rho-Rock activity in MHBS and MHBC. We found that this treatment stalled apical nuclear migration only in MHBS, as seen for the morphologically similar hindbrain tissue but not in the MHBC (Fig. S4 H). This confirmed that tissue shape is linked to the mechanisms of apical nuclear migration.

We further tested whether a change in cell and tissue morphology would influence apical nuclear migration mechanisms. To this end, we used a previously published laminin α-1 morpholino (Pollard et al., 2006) that was shown to give rise to flat retinal neuroepithelia (Sidhaye and Norden, 2017). We confirmed that this treatment led to changes in retinal cell shape in a dose-dependent manner (Fig. S4 E). Higher doses of the laminin α-1 morpholino resulted in straighter retinal tissue shape (Fig. 6 A) and more cylindrical retinal cell shape (Fig. 6 B and Fig. S4 E). In embryos treated with lower doses of laminin α-1 morpholino, a basal actin cloud was still observed in G2, and nuclei moved toward apical positions (n = 4; Fig. 6 B and Video 10). In embryos treated with a higher morpholino dose no cytoplasmic actin enrichment was observed in most cells and actin was seen more laterally. In this case, nuclei either did not move apically in G2 (n = 2) or nevertheless reached apical positions, most likely using a different mechanism (n = 3; Fig. 6 B and Video 10).

These results indicate that indeed cell and tissue shape are linked to apical nuclear migration mechanisms. When atypical shape changes occur within the tissue, the cytoskeletal machinery is able to at least partially adapt to ensure apical nuclear migration.

We conclude that cell and tissue shape influence the actin-dependent mechanisms that move nuclei apically in similar tissues within the same organism. The fact that actin is differently regulated in differently shaped neuroepithelia to achieve the same goal stresses the robustness of apical nuclear migration in diverse pseudostratified tissues.

Discussion

Our study demonstrates that the cytoskeletal force-generating mechanisms for nuclear positioning vary in similar tissues within the same organism depending on cell and tissue geometry. In particular, we found that apical nuclear migration in pseudostratified neuroepithelia of different cell and tissue shape is driven by distinct actomyosin-dependent force-generating mechanisms. We propose that an actomyosin contractility-dependent mechanism, downstream of the Rho-ROCK pathway, acts in the straight hindbrain tissue (Fig. 6 C). In contrast, in the retinal tissue that shows basally constricted morphology and a corresponding basal actomyosin accumulation, nuclei are possibly pushed by a formin-nucleated expanding actin network (Fig. 6 C). These mechanisms are conserved in tissues of similar shape, and changes in cell morphology can lead to adaptation of mechanisms to ensure successful apical nuclear migration.

Prerequisites and possible mechanisms of apical nuclear migration

We showed that nuclei in hindbrain and retina are highly deformable. This is most likely due to their lack of Lamin A/C expression, a major contributor to nuclear mechanical stiffness (Swift et al., 2013). Retinal and hindbrain nuclei display frequent deformations in all phases of the cell cycle, providing further evidence that their nuclear envelopes are relatively soft. These deformations are most prominent during nuclear apical migration in the retinal neuroepithelium. Future studies are needed to test whether the observed deformability of nuclei in neuroepithelia enable the complex nuclear migration patterns occurring in these highly proliferative epithelia. With developmental progression, the epithelium becomes more and more crowded (Matejčić et al., 2018), which means that nuclei need to squeeze through increasingly confined spaces. Here, nuclear deformability could help to ensure successful apical migration.

Interestingly, the mechanisms driving apical nuclear migration vary depending on tissue. Apical nuclear migration in hindbrain cells is driven by ROCK activity. This could mean that nuclear movements depend on ROCK-induced cortical contractility, as previously implicated in apical nuclear migration in *Drosophila* wing disc (Meyer et al., 2011). One possible contractility-dependent mechanism is the generation of cortical flows, similar to those in *C. elegans* zygotes and cells undergoing adhesion-free migration (Munro et al., 2004; Mayer et al., 2010; Bergert et al., 2015). Gradual contraction of the cortex due to the action of a multitude of myosin motors could further explain the faster and smoother nuclear migration in hindbrain. Future experiments, including specific perturbation of cortical contractility, will help to test this hypothesis.

In the retina, basal enrichment of actin and myosin in G2 was reported previously (Norden et al., 2009; Leung et al., 2011), and it was proposed that nuclei are propelled by basal process constriction. However, we did not observe such constriction during apical migration of retinal nuclei (Fig. 1 C, Fig. 3 A, and Videos 1 and 4). Furthermore, we did not observe a strong enrichment of active myosin in the cell cortex, which makes it unlikely that cortical flows are the main driver of apical nuclear migration in the retina. In contrast, the periodic enrichment of actomyosin that closely follows nuclei during movement and the accompanying nuclear deformations argue that an expanding actin network could push the nucleus apically.

Such a pushing mechanism has not yet been described for nuclear migration in developing tissues. However, it has been shown that polymerizing actin networks can generate saltatory movements in vitro (Delatour et al., 2008), for the motility of intracellular parasites (Gerbal et al., 2000; Soo and Theriot, 2005) and during the pushing of chromosomes in mouse oocytes (Li et al., 2008; Yi et al., 2013).

To formalize how polymerizing actin could generate the forces necessary for nuclear migration in neuroepithelial cells, we developed a proof-of-principle theoretical model (see Online supplemental text and Fig. 4 I). Our mathematical model suggests that cortex-anchored bundled f-actin could explain the observed phenomena. Cell geometry can direct f-actin growth, with frustum-shaped cells preferentially growing f-actin into

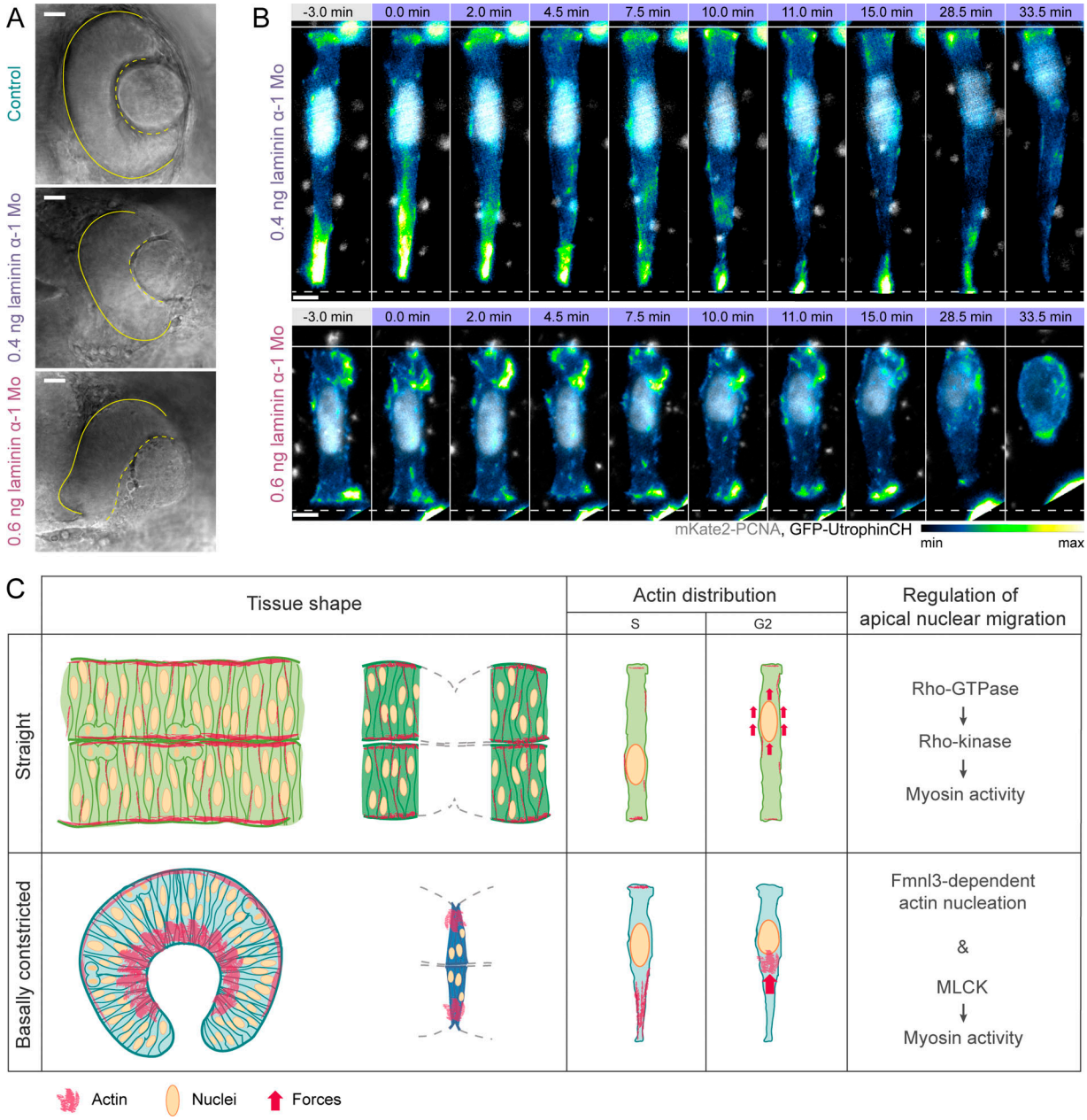

Figure 6. **Tissue shape and the force generation mechanisms of apical nuclear migration are likely linked by the distinct actomyosin distribution in straight and basally constricted tissues. (A)** Retinal tissue morphology in control and laminin α-1 morphant (laminin α-1 Mo) embryos, injected with different amounts of morpholino. **(B)** Representative time series of retinal cell morphology and actin distribution during apical migration in laminin α-1 morphant embryos, injected with different amounts of morpholino (shown is the maximum projection of all z planes in the 3D stack; Video 10). mKate2-PCNA labels nuclei (gray), and GFP-UtrophinCH labels actin (lookup table indicates minimal and maximal GFP-UtrophinCH signal values). Scale bars: 10 µm (A), 5 µm (B). **(C)** Schematic summary of suggested links between tissue shape and mechanisms of apical nuclear migration. Straight and basally constricted tissues show different distributions of actomyosin. In straight tissues, actomyosin is evenly distributed along the lateral sides of cells. An enrichment of actomyosin is observed basolaterally in basally constricted tissues. A basal actomyosin network that pushes the nucleus to the apical side could thus only be formed in cells of basally constricted but not straight tissues.

the cytoplasm directed toward the larger side (Reymann et al., 2010). Furthermore, active myosin (including myosin II) has been shown to selectively contract and disassemble antiparallel actin structures, promoting the growth and likely cross-linking of parallel actin bundles in vitro (Reymann et al., 2012). A similar mechanism could be at play in the retinal neuroepithelium, where actin bundles growing via formin-catalyzed polymerization at the anchored end push the nucleus toward the apical side by direct contact against the nuclear envelope. Intriguingly, the model shows that for appropriate parameter ranges (taken from the literature [Gittes et al., 1993; Kalwarczyk et al., 2011] and our own observations), the critical length for Euler buckling of the bundle (Kierfeld et al., 2006; Bathe et al., 2008) is consistent with the observed trailing distance of the

formin enrichment zone behind the nucleus (Online supplemental text). Further, as the nucleus encounters spatial constraints, the effective dynamic viscosity would rise, resulting in a decreased buckling length threshold. As filaments then buckle, the continued addition of actin monomers at the trailing formin sites provides increased forces to the nucleus due to the rising stresses in the filaments, eventually squeezing the nucleus through. The buckled filaments and bundles then straighten, leading to a burst of increased velocity. A key prediction of this proof-of-principle model is that the average velocity of the nucleus is dominated by the speed of formin-catalyzed f-actin polymerization (Hotulainen and Lappalainen, 2006). Indeed, we observe that these are in close concert (Fig. 1 G, Fig. S4 G, Table 1, and Online supplemental text). The possibility that the coordinated expansion of the actin network pushes the nucleus apically is an exciting new mechanism for positioning nuclei. It should be stressed, however, that this model is currently based only partly on measured parameters and that some parameters, while consistent with the literature, still need to be explored. Furthermore, at this point we explicitly do not exclude the possibility that force could also be generated by a contractility-based mechanism. Further experiments investigating the actomyosin network organization are necessary to validate or exclude either of these possibilities. Thus, testing and expanding the current models will be important to clarify the mechanisms of nuclear migration in basally constricted tissues.

The actin-dependent mechanisms used for apical nuclear migration depend on tissue geometry

Our finding that neuroepithelial cells in tissues with different morphology use distinct actin-dependent mechanisms for apical nuclear movements demonstrates that the actomyosin cytoskeleton can use diverse means of force generation depending on cell and tissue context when performing a task critical for cell function and tissue development. Interestingly, actomyosin is responsible for both cell and tissue shape generation and maintenance, as well as the generation of the intracellular forces during nuclear positioning. Hindbrain and retinal neuroepithelia differ in cell and tissue shape as well as in tissue-wide cytoskeleton organization (Fig. 5, A, A', and B; Sidhaye and Norden, 2017; Matejčić et al., 2018). It is tempting to speculate that intracellular actin distribution, related to tissue shape, influences the force generation mechanism for apical nuclear migration. The tissue-wide basal enrichment of actomyosin, important for basal constriction and thereby development of the hemispheric retina (Nicolás-Pérez et al., 2016; Sidhaye and Norden, 2017), could favor the formation of the basal structures that push the nucleus apically (Fig. 6 C). Such basal actin enrichment and basal cell constriction could further make a pushing mechanism more efficient by providing a stable base to push against. Actomyosin enrichment is absent in the hindbrain, where, accordingly, a different mechanism is used (Fig. 6 C). Of note, this basal actomyosin bias creates a region in the tissue that is inaccessible for nuclei, and this could also explain the more apical starting points of nuclei in the retina compared with hindbrain (Matejčić et al., 2018).

To probe whether and how the cytoskeleton moves nuclei in other epithelial architecture regimes, more studies of apical nuclear migration are needed. It is, for example, not known whether mechanisms differ in apically constricted hindbrain regions or in tissues that thicken over development, like the more mature retinal neuroepithelium (Matejčić et al., 2018). Apical nuclear migration is a prerequisite for apical mitosis and, hence, correct tissue development in all pseudostratified epithelia. As these tissues are the precursors of organs in diverse organisms (Norden, 2017), cytoskeletal adaptability to move nuclei depending on the surroundings is most likely crucial for successful organogenesis. The variety of the described mechanisms of apical nuclear migration across systems suggests that, for pseudostratified epithelial cells, this important end justifies the many means.

Materials and methods

Zebrafish husbandry

Wild-type zebrafish were maintained and bred at 26°C. Embryos were raised at 21°C, 28.5°C, or 32°C in E3 medium. Animals were staged in hours post fertilization according to Kimmel et al. (1995). From 8 h post fertilization (hpf), the medium was supplemented with 0.2 mM 1-phenyl-2-thiourea (Sigma-Aldrich) to prevent pigmentation. Embryos were anesthetized in 0.04% tricaine methanesulfonate (MS-222; Sigma-Aldrich) before live imaging. Live imaging was performed for 6–14 h from 18 hpf for the hindbrain and MHB, and from 24 hpf for the retina. All animal work was performed in accordance with European Union directive 2010/63/EU, as well as the German Animal Welfare Act.

RNA and DNA injections

To mosaically label cells in zebrafish neuroepithelia, DNA constructs were injected into 1-cell-stage embryos, while mRNA was injected into the cytoplasm of a single blastomere of 32–128-cell-stage embryos. DNA was injected at 10–25 pg per embryo. mRNA was synthesized using the Ambion mMessage mMachine kit and injected at 40 to 100 pg per embryo. The injection mix was prepared in water, and the injected volume was 0.5–1.0 nl. A full list of the constructs used can be found in Table S1.

Cloning strategies

Gateway cloning (Thermo Fisher Scientific) based on the Tol2 kit (Kwan et al., 2007) was used for all constructs.

pCS2+ mKate2-PCNA

The human PCNA coding sequence was amplified from pCS2+ GFP-PCNA (Leung et al., 2011), and a 3′-entry clone was generated. It was combined with mKate2 p5ENTR(L1-L2) (a kind gift from Andrew Oates, École polytechnique fédérale de Lausanne, Lausanne, Switzerland) and pCS2+ pDEST(R1-R3) (Villefranc et al., 2007).

T2 heat shock promoter 70 (hsp70):EGFP-LAP2b

The rat LAP2b coding sequence was amplified from a pmRFP_LAP2beta_IRES_puro2b plasmid (Steigemann et al.,

2009; 21047; Addgene), and a 3′-entry clone was generated. It was combined with hsp70 promoter p5ENTR(L4-R1) clone (Kwan et al., 2007), EGFP pMENTR(L1-L2) (Villefranc et al., 2007), and GW Tol2-pA2 p DEST backbone (Villefranc et al., 2007).

T2-hsp70:LMNA-mKate2

RNA was extracted from embryos 24 hpf using the TRI Reagent (Sigma-Aldrich) according to the manufacturer's protocol. cDNA was synthesized using a first strand cDNA synthesis kit (Fermentas/Thermo Fisher Scientific). The zebrafish lamin A (NCBI accession number BC163807.1) coding sequence was amplified from zebrafish cDNA to generate a middle-entry clone without a stop codon at the end. The following primers were used: 5′-GGGGACAAGTTTGTACAAAAAAGCAGGCTGGGAGTCGCAGCACACACTCTTT-3′ and 5′-GGGGACCACTTTGTACAAGAAAGCTGGGTCAATAGAGCAGTTGTCCACTTTGG-3′. The middle-entry clone was combined with an hsp70 promoter p5ENTR(L4-R1) clone (Kwan et al., 2007), mKate2 p3ENTR(R2-L3) (a kind gift from Andrew Oates), and GW Tol2-pA2 p DEST backbone (Villefranc et al., 2007).

T2-hsp70:Fmnl3ΔC-EGFP

The middle-entry clone for truncated Fmnl3, lacking catalytic C-terminal FH1, FH2, and DAD domains (pME-Fmnl3ΔC;Phng et al., 2015), was a kind gift from Li-Kun Phng (RIKEN Center for Biosystems Dynamics Research, Kobe, Japan). It was combined with hsp70 promoter p5ENTR(L4-R1) clone (Kwan et al., 2007), EGFP p3ENTR(R2-L3) (Villefranc et al., 2007), and GW Tol2-pA2 p DEST backbone (Villefranc et al., 2007).

T2-hsp70:Fmnl3-EGFP

The zebrafish Fmnl3 (GenBank accession number NM_001346154) coding sequence was amplified from zebrafish cDNA to generate a middle-entry clone without a stop codon at the end. The following primers were used: 5′-GGGGACAAGTTTGTACAAAAAAGCAGGCTGGATGGGGAATATTGAGAGTGTGG-3′ and 5′-GGGGACCACTTTGTACAAGAAAGCTGGGTCGCAGATGGACTCGTCGAAGA-3′. The middle-entry clone was combined with hsp70 promoter p5ENTR(L4-R1) clone (Kwan et al., 2007), mKate2 p3ENTR(R2-L3) (a kind gift from Andrew Oates), and GW Tol2-pA2 p DEST backbone (Villefranc et al., 2007).

T2-hsp70:DN-Rok2-EGFP

The DN-Rok2 (Marlow et al., 2002) sequence was amplified to generate a middle-entry clone. It was combined with hsp70 promoter p5ENTR(L4-R1) clone (Kwan et al., 2007), mKate2 p3ENTR(R2-L3) (a kind gift from Andrew Oates), and GW Tol2-pA2 p DEST backbone (Villefranc et al., 2007).

Heat shock of embryos

To induce expression of the hsp70–driven constructs, embryos were incubated in a water bath at 17 hpf for imaging the hindbrain and at 23 hpf for imaging the retina to induce expression. The heat shock lasted 20 min at 37°C for Hsp70:DN-Rok2-EGFP and 30 min at 39°C for Hsp70:NWASP-CA-mKate2 and Hsp70:Fmnl3-EGFP. For induction of Hsp70:Fmnl3ΔC-EGFP, heat shock lasted 15 min at 39°C for imaging the hindbrain neuroepithelium and for 20 min at 39°C when imaging the retinal neuroepithelium.

Morpholino experiments

To knock down gene function, the following amounts of morpholinos were injected into the yolk at 1-cell stage to manage apoptosis: 0.4 or 0.6 ng laminin α-1 MO, 5′-TCATCCTCATCTCCATCATCGCTCA-3′ (Pollard et al., 2006), and 2 ng p53 MO, 5′-GCGCCATTGCTTTGCAAGAATTG-3′ (Robu et al., 2007).

Drug treatments

All inhibitors were dissolved in DMSO, except latrunculin A, which was dissolved in ethanol. Equal volumes of DMSO or ethanol as the stock inhibitor solution were used for control treatments. Dechorionated embryos were treated by incubation in E3 medium containing the inhibitors at their respective working concentrations (Table S2), either in plastic multi-well plates or in compartmentalized 35-mm glass bottom Petri dishes (Greiner Bio-One). All treatments were started after 17 hpf for the hindbrain and after 23 hpf for the retina.

Myosin perturbation for fixed imaging

Before fixation, embryos were incubated for 6 h in DMSO, 125 µM Rockout, and 100 µM ML-7 and for 3 h in 100 µM blebbistatin.

Live imaging of chemical perturbations

Embryos were dechorionated and pretreated for 1 h before mounting the sample. Concentrations for pretreatment were 100 µM Rhosin, 25 µM Y16, 100 µM Rockout, 200 µM ML-7, 175 µM CK-666, and 10 µM SMIFH2. After mounting in agarose in glass-bottom dishes, embryos were incubated in the inhibitor concentrations listed in Table S2 for 14 h and imaged using a spinning disk confocal microscope (SDCM).

Cells that completed S phase were counted using the Cell-Counter plugin in Fiji (Schindelin et al., 2012). Only embryos in which the drugs had an effect were analyzed. The numbers of treated and affected embryos are found in Table S3. Representative trajectories for controls and Rockout- and SMIFH2-treated cells were generated using the MTrackJ Fiji plugin.

Immunofluorescence

For whole-mount immunostainings, embryos were fixed in 4% PFA (Sigma-Aldrich) in PBS for actomyosin and nuclear imaging, and Dent's fixative for lamin immunostaining. The embryos were permeabilized with trypsin (this step was omitted when Dent's fixation was used), blocked, and incubated with the primary antibody for 3 d and later with the appropriate fluorescently labeled secondary antibody for 3 d. The following antibodies and probes were used: primary antibodies—1:50 anti-phospho-myosin (Cell Signaling Technology Cat# 3671, RRID: AB_330248; Lot#6), 1:500 anti-pH3 (Abcam Cat# ab10543, RRID: AB_2295065; Lot# GR253717-7), 1:200 anti-Lamin A/C (Abcam Cat# ab8984, RRID: AB_306913; Lot#GR3257084-1), and 1:200 anti-Lamin B1 (Abcam Cat# ab16048, RRID: AB_10107828; Lot#GR3244896-2); secondary antibodies and fluorescent

markers—1:500 Alexa Fluor 647 anti-rat (Thermo Fisher Scientific Cat# A-21247, RRID: AB_141778), 1:500 Alexa Fluor 488 anti-rabbit (Thermo Fisher Scientific Cat# A-11070, RRID: AB_2534114; Lot#1705868), 1:500 Alexa Fluor 488 anti-mouse (Thermo Fisher Scientific Cat# A-21200, RRID: AB_2535786; Lot#1877470), 1:500 Alexa Fluor 594 anti-rabbit (Thermo Fisher Scientific Cat# A-11072, RRID: AB_2534116), 1:50 Alexa Fluor 488 Phalloidin (Thermo Fisher Scientific Cat# A12379, RRID: AB_2315147; Lot#1737901), 1:50 Rhodamine-Phalloidin (Thermo Fisher Scientific Cat# R415, RRID: AB_2572408; Lot#1321031), and DAPI (Thermo Fisher Scientific Cat# D1306, RRID: AB_2629482).

Microscope image acquisition

Experiments were conducted between 18 and 30 hpf in the hindbrain and between 24 and 36 hpf in the retina before full onset of neurogenesis for each tissue.

Confocal scans

Fixed samples were imaged on an LSM 880 inverted point scanning confocal system (Carl Zeiss Microscopy) using the 40×/1.2 C-Apochromat water immersion objective (Carl Zeiss Microscopy). Samples were mounted in 1% agarose in glass bottom dishes (MatTek) or compartmentalized glass bottom dishes (Greiner Bio-One) filled with PBS and imaged at room temperature. Acquired z stacks had a thickness of 20–36 µm and step size of 0.75–1 µm. The microscope was operated by ZEN 2 (black edition) software.

Time-lapse imaging using an SDCM

Live imaging of apical migration perturbations was done using an Andor SDCM system. The spinning disk setup consisted of an IX71 microscope (Olympus) and CSU-X1 scan head (Yokogawa). The samples were mounted in compartmentalized glass bottom dishes (Greiner Bio-One) or glass bottom dishes (MatTek) into 0.9% agarose in E3 medium containing 0.1 M Hepes (pH 7.25) and 0.01% MS-222 (Sigma-Aldrich). The dish was filled with E3 medium containing 0.01% MS-222 (Sigma-Aldrich). Imaging was performed with a UPLSAPO 60x/1.5 water immersion objective (Olympus) and Neo sCMOS camera (Andor) at 28.5°C regulated by an environmental chamber. A z stack of thickness 35–36 µm was acquired with 1-µm steps. Images were taken every 5–7 min for 12–14 h. The microscope was operated by Andor iQ 3.0 software.

Time-lapse imaging using LSFM

Imaging of single labeled cells in the hindbrain, retina, and MHB was performed as previously described (Icha et al., 2016b) using the Lightsheet Z.1 (Carl Zeiss Microscopy). The sample chamber was filled with E3 medium containing 0.01% MS-222 (Sigma-Aldrich) and 0.2 mM N-phenylthiourea (Sigma-Aldrich) and maintained at 28.5°C. The embryos were embedded in a 0.9% agarose column, and a 25–35-µm z stack of the hindbrain, retina, or MHB was acquired with 1-µm steps in a single-view, single-sided illumination mode. Images were taken every 0.25–1 min for 3–4 h using the Plan-Apochromat 40×/1.0-W detection objective (Carl Zeiss Microscopy) and the two PCO.Edge 5.5 sCMOS cameras. The microscope was operated by ZEN 2014 (black edition) software.

Laser ablations

Nuclei were labeled with H2B-RFP to visualize shifts in chromatin distribution, and GFP-PCNA was used as a cell cycle marker. As PCNA is also recruited to sites of DNA damage (Aleksandrov et al., 2018), its enrichment at the ablated region served as a confirmation for successful ablation. Nuclei were ablated in S phase or several minutes after the onset of G2. A region of interest, consisting of a single point, was selected in the center of each nucleus, resulting in a circular ablated region. 12 µm (16 z planes) of the tissue surrounding the region of interest was acquired before ablation during three time points 10 s apart. 20 repeats of the laser pulse with a frequency of 30 Hz were performed on the region of interest. 12 µm (16 z planes) of the tissue surrounding the cut was scanned for 5–15 min with temporal resolution of 10 s to record the deformations of the ablated region in the hindbrain and the retina after the cut. The shape of the ablated regions was only considered in the first 30 s after ablation due to the assumption that later on the damage inflicted by laser ablation might lead to interruption of the force-generating process.

The deformations of the ablated regions were assessed by counting the number of nuclei in which a basal indentation was visible in the z plane in the center of the nucleus.

In situ hybridization

Riboprobes were generated from cDNA templates, and in situ hybridization was performed as previously described (Thisse et al., 1993; Oates and Ho, 2002). The following primers were used to generate the probes for Fmnl3 (lowercase bases contain T7 polymerase promoter): probe 1, 5′-ATCACATAGGGTGGGTTCGC-3′ and 5′-taatacgactcactatagGGATGACTGCCAGCTCCTTGTC-3′; probe 2, 5′-GAGCAAGGTCTCCCAGAAGG-3′ and 5′-taatacgactcactatagGGATTGTTAAAGGCCTCCTCCGC-3′; sense probe, 5′-ATTGTTAAAGGCCTCCTCCGC-3′ and 5′-taatacgactcactatagGGGAGCAAGGTCTCCCAGAAGG-3′. Whole-mount stained embryos were documented using an Olympus SZX12 stereomicroscope equipped with a Micropublisher 5.0 RTV camera (QImaging).

Image analysis

Minimal image processing was used, before image analysis. Processing consisted of image cropping in ZEN and/or Fiji (Schindelin et al., 2012), bleach correction and/or background subtraction, and drift correction using Fiji. After image analysis in Imaris 8 or 9 (BitPlane) or Fiji, data were analyzed and plotted using Microsoft Excel, GraphPad Prism, or BoxPlotR (Spitzer et al., 2014). Statistical analysis was performed using GraphPad Prism and MATLAB.

Sample drift correction

Sample drift in 3D stacks was corrected using a Fiji plugin created by Benoit Lombardot (Scientific Computing Facility, Max Planck Institute of Molecular Cell Biology and Genetics, Dresden, Germany). The script can be found on http://imagej.net/Manual_drift_correction_plugin.

Analysis of apical nuclear migration kinetics

The beginning of G2 was defined by the disappearance of PCNA foci, indicating the end of S phase, until the onset of cell rounding (Leung et al., 2011). Apical migration was defined by the beginning of directed motion of the nucleus toward the apical side after the onset of G2 and before the onset of cell rounding.

To generate cell trajectories for instantaneous velocities, mean square displacement, and directionality ratio analysis, nuclei were tracked in 3D using Imaris 8 or 9 (Bitplane) during S phase and G2 phase. Data points were taken at 1-min intervals. The cell axis was defined by the positions of the apical and basal endpoints, measured in 3D in the last time point of S phase for each cell. Nuclear position was projected onto the cell axis, obtaining one-dimensional time series, as described previously (Norden et al., 2009; Leung et al., 2011). Resulting trajectories were analyzed in MATLAB as described previously (Norden et al., 2009; Leung et al., 2011). The kurtosis of instantaneous velocity distributions was calculated using GraphPad Prism.

Nuclear segmentation, shape measurements, and tracking in 3D

Semiautomatic segmentation and tracking were performed on 3D stacks in time series of single-labeled migrating nuclei using the Surface tool in Imaris 8 or 9 (Bitplane). The position of the nuclear centroid over time in 3D was extracted. In addition, an ellipsoid was fitted in the segmented surface in each time point by the software, enabling the extraction of the length of the semi-axes of the nucleus. The nuclear aspect ratio (A/C) was calculated by dividing the length of each of the short semi-axes by the length of the long semi-axis, C.

The average nuclear aspect ratio during S phase was calculated for each nucleus (A/C_0) and used to calculate the value of the normalized aspect ratio for each time point in G2 (A/C_{normi}) following the formula:

$$A/C_{normi} = \frac{A/C_i - A/C_0}{A/C_0},$$

where A/C_i is the nuclear aspect ratio measured in each time point (t_i).

Normalized aspect ratios for each time point were pooled for all cells originating from the same tissue.

Tissue and cell shape measurements

Single cell length measurement in 3D. The 3D viewer of Imaris 8 or 9 (Bitplane) was used to visualize labeled cells in 3D. The positions of the edges of the apical and basal surface were defined using the Measurement Point tool in the last time point of S phase before the onset of migration. A custom MATLAB script was used to calculate the distance between the apical and basal surface of each cell, and this distance was taken as the length of the cell.

Measurement of apical and basal cell footprint areas. Apical and basal cell footprints were segmented semiautomatically in Fiji. Linear regions of interest covering the apical and basal footprint, respectively, of S-phase cells were drawn to re-slice the 3D stack and generate 2D stacks of the cell endfeet of at least four time points, 1 min apart. The footprints were segmented using automatic thresholding (Huang and Wang, 1995) using the stack histogram; selections were created, and their area was measured every minute for 4–10 min.

Quantifications of actin distribution

Tissue-wide actin, myosin, and nuclear distribution profiles. The average fluorescent intensity distribution of phalloidin, phosphomyosin, and DAPI along the apicobasal cell axis was measured as described previously (Sidhaye and Norden, 2017; Matejčić et al., 2018). Regions of interest were defined as a 10 µm × 10 µm × (tissue thickness) cuboid for retina and hindbrain and 5 µm × 5 µm × (tissue thickness) cuboid for MHBS and MHBC. 6–10 profiles originating from four to six samples were measured from each tissue.

Actin distribution profiles basal of the nucleus. Basal nuclear actin distribution profiles in hindbrain and retinal cells were measured in Fiji using the region of interest immediately basal of the nucleus in each time point. The actin signal intensity in the central z plane of the cell was measured and normalized to the minimum and the maximum for a given time point. The profiles from all time points in G2 were used to calculate the average actin profile for the hindbrain and retinal cells.

Analysis of basal actin oscillations and cross-correlation analysis. Average basal actin intensity was measured in a square region of interest in the SUM projection of each retinal cell for the duration of G2 using Fiji. Average actin intensity was normalized to the total actin signal in the cell for each time point. Data were sampled at intervals of 0.5 min. The rises and plateaus in actin signal, instantaneous velocity, and nuclear aspect ratio were detected, and their frequency was calculated as the reciprocal average time difference between the detections, for each time series using MATLAB. Both points of increase and stagnation were detected, as these were considered to represent biologically relevant maintenance of actin pulses and apical migration. The fluctuations of basal actin were cross-correlated with the fluctuations of mean instantaneous velocity and aspect ratio using MATLAB's xcorr function. Prior to cross-correlating, each time series was scaled by subtracting its mean and dividing by the standard deviation. A lag of maximal 3 min was allowed. Maximum cross-correlation values and the corresponding time lags were used for analysis.

Statistical analysis

Statistical tests and definitions of error bars are indicated in the figure legends. All statistical tests were two sided. P values >0.05 were considered not significant. All P values are indicated in the corresponding tables or figure legends. Sample sizes are listed in Tables S3, S4, and S5. Statistical analyses were performed using Prism 7 (GraphPad) software and MATLAB.

Online supplemental material

Fig. S1 shows kinetics of a comparison between hindbrain and retinal G2 nuclei, a positive control Lamin A/C immunostaining in the tail, and the fluctuations in nuclear shape and velocity in G2. It further shows the different deformations of ablated nuclear regions in hindbrain and retina. Fig. S2 shows chemical

perturbation of the cytoskeleton in hindbrain and retina, the distribution of actin and myosin, and the fluctuations in basal actin in the retina. Fig. S3 shows chemical perturbations of actomyosin and a summary of all cytoskeleton perturbations used. Fig. S4 shows genetic perturbation of Arp2/3, *fmnl3* in situ hybridization, cell morphology, and nuclear kinetics characterization, as well as perturbation of ROCK in MHB. Video 1 shows apical nuclear migration in a hindbrain and retinal cell. Video 2 shows nuclear deformations in interphase. Video 3 shows the effects of chemical perturbation of the cytoskeleton on apical nuclear migration in hindbrain and retina. Video 4 shows actin distribution in hindbrain and retinal G2 cells. Video 5 shows the effects of chemical perturbation of ROCK or formins on apical nuclear migration in hindbrain and retina. Video 6 shows the effects of chemical perturbation of Rho-kinase, MLCK, or Arp2/3 on apical nuclear migration in hindbrain and retina. Video 7 shows the effects of genetic perturbation of ROCK, Fmnl3, or Arp2/3 on apical nuclear migration in hindbrain and retina. Video 8 shows Fmnl3 distribution in hindbrain and retinal cells. Video 9 shows actin distribution in MHBS and MHBC G2 cells, as well as the effect of chemical perturbation of ROCK on apical migration. Video 10 shows actin distribution in retinal G2 cells of laminin morphants. A proof-of-principle theoretical model for apical nuclear migration is described in detail in the supplemental text. Table S1 lists constructs and Table S2 lists cytoskeleton inhibitors. Table S3 shows the number of embryos and cells used in the analysis comparing different parameters in hindbrain and retina. Table S4 shows the number of embryos and cells used in the analysis comparing different parameters in hindbrain, retina, MHBS, and MHBC. Table S5 shows the number of instances in which different unquantified observations were made.

Acknowledgments

We thank the Norden laboratory, J. Brugués, S. Grill, and especially G. Salbreux for fruitful project discussion. J. Icha, N. Kirkland, Y-L. Mao, and P. Strzyz are thanked for helpful comments on the manuscript. We are grateful to H. Hollak, G. Jurado, S. Kaufmann, J. Sidhaye, the Light Microscopy Facility, Scientific Computing, and the Fish Facility of the Max Planck Institute of Molecular Cell Biology and Genetics for experimental help. We thank Li-Kun Phng for sharing the Fmnl3ΔC construct.

I. Yanakieva was a member of the International Max Planck Research School for Cell, Developmental, and Systems Biology and recipient of an ELBE PhD fellowship. C. Norden was supported by the Max Planck Institute of Molecular Cell Biology and Genetics and the German Research Foundation (NO1068/1-1 and NO1068/3-1).

The authors declare no competing financial interests.

Author contributions: C. Norden and I. Yanakieva conceptualized and decided on the methodology used in this work. I. Yanakieva performed the majority of the experiments and analysis. M. Matejčić helped with the experiments. A. Erzberger and M. Matejčić designed the analysis tools and performed the analysis. C.D. Modes generated the model. C. Norden and I. Yanakieva wrote the manuscript with the help of all the other authors.

Submitted: 24 January 2019
Revised: 29 May 2019
Accepted: 18 July 2019

References

Aleksandrov, R., A. Dotchev, I. Poser, D. Krastev, G. Georgiev, G. Panova, Y. Babukov, G. Danovski, T. Dyankova, L. Hubatsch, et al. 2018. Protein dynamics in complex DNA lesions. *Mol. Cell.* 69:1046–1061.e5. https://doi.org/10.1016/j.molcel.2018.02.016

Bathe, M., C. Heussinger, M.M. Claessens, A.R. Bausch, and E. Frey. 2008. Cytoskeletal bundle mechanics. *Biophys. J.* 94:2955–2964. https://doi.org/10.1529/biophysj.107.119743

Bergert, M., A. Erzberger, R.A. Desai, I.M. Aspalter, A.C. Oates, G. Charras, G. Salbreux, and E.K. Paluch. 2015. Force transmission during adhesion-independent migration. *Nat. Cell Biol.* 17:524–529. https://doi.org/10.1038/ncb3134

Bertipaglia, C., J.C. Gonçalves, and R.B. Vallee. 2018. Nuclear migration in mammalian brain development. *Semin. Cell Dev. Biol.* 82:57–66. https://doi.org/10.1016/j.semcdb.2017.11.033

Cho, S., M. Vashisth, A. Abbas, S. Majkut, K. Vogel, Y. Xia, I.L. Ivanovska, J. Irianto, M. Tewari, K. Zhu, et al. 2019. Mechanosensing by the lamina protects against nuclear rupture, DNA damage, and cell-cycle arrest. *Dev. Cell.* 49:920–935.e5. https://doi.org/10.1016/j.devcel.2019.04.020

Delatour, V., E. Helfer, D. Didry, K.H. Lê, J.F. Gaucher, M.F. Carlier, and G. Romet-Lemonne. 2008. Arp2/3 controls the motile behavior of N-WASP-functionalized GUVs and modulates N-WASP surface distribution by mediating transient links with actin filaments. *Biophys. J.* 94:4890–4905. https://doi.org/10.1529/biophysj.107.118653

Fridolfsson, H.N., and D.A. Starr. 2010. Kinesin-1 and dynein at the nuclear envelope mediate the bidirectional migrations of nuclei. *J. Cell Biol.* 191:115–128. https://doi.org/10.1083/jcb.201004118

Gerbal, F., P. Chaikin, Y. Rabin, and J. Prost. 2000. An elastic analysis of *Listeria monocytogenes* propulsion. *Biophys. J.* 79:2259–2275. https://doi.org/10.1016/S0006-3495(00)76473-3

Gittes, F., B. Mickey, J. Nettleton, and J. Howard. 1993. Flexural rigidity of microtubules and actin filaments measured from thermal fluctuations in shape. *J. Cell Biol.* 120:923–934. https://doi.org/10.1083/jcb.120.4.923

Gomes, E.R., S. Jani, and G.G. Gundersen. 2005. Nuclear movement regulated by Cdc42, MRCK, myosin, and actin flow establishes MTOC polarization in migrating cells. *Cell.* 121:451–463. https://doi.org/10.1016/j.cell.2005.02.022

Gundersen, G.G., and H.J. Worman. 2013. Nuclear positioning. *Cell.* 152:1376–1389. https://doi.org/10.1016/j.cell.2013.02.031

Gutzman, J.H., E.G. Graeden, L.A. Lowery, H.S. Holley, and H. Sive. 2008. Formation of the zebrafish midbrain-hindbrain boundary constriction requires laminin-dependent basal constriction. *Mech. Dev.* 125:974–983. https://doi.org/10.1016/j.mod.2008.07.004

Harada, T., J. Swift, J. Irianto, J.-W. Shin, K.R. Spinler, A. Athirasala, R. Diegmiller, P.C.D.P. Dingal, I.L. Ivanovska, and D.E. Discher. 2014. Nuclear lamin stiffness is a barrier to 3D migration, but softness can limit survival. *J. Cell Biol.* 204:669–682. https://doi.org/10.1083/jcb.201308029

Hotulainen, P., and P. Lappalainen. 2006. Stress fibers are generated by two distinct actin assembly mechanisms in motile cells. *J. Cell Biol.* 173:383–394. https://doi.org/10.1083/jcb.200511093

Hu, D.J., A.D. Baffet, T. Nayak, A. Akhmanova, V. Doye, and R.B. Vallee. 2013. Dynein recruitment to nuclear pores activates apical nuclear migration and mitotic entry in brain progenitor cells. *Cell.* 154:1300–1313. https://doi.org/10.1016/j.cell.2013.08.024

Huang, L.-K., and M.-J.J. Wang. 1995. Image thresholding by minimizing the measures of fuzziness. *Pattern Recognit.* 28:41–51. https://doi.org/10.1016/0031-3203(94)E0043-K

Icha, J., C. Kunath, M. Rocha-Martins, and C. Norden. 2016a. Independent modes of ganglion cell translocation ensure correct lamination of the zebrafish retina. *J. Cell Biol.* 215:259–275. https://doi.org/10.1083/jcb.201604095

Icha, J., C. Schmied, J. Sidhaye, P. Tomancak, S. Preibisch, and C. Norden. 2016b. Using light sheet fluorescence microscopy to image zebrafish eye development. *J. Vis. Exp.* 110:e53966.

Icha, J., M. Weber, J.C. Waters, and C. Norden. 2017. Phototoxicity in live fluorescence microscopy, and how to avoid it. *BioEssays.* 39:1700003. https://doi.org/10.1002/bies.201700003

Jung, H.J., C. Coffinier, Y. Choe, A.P. Beigneux, B.S. Davies, S.H. Yang, R.H. Barnes II, J. Hong, T. Sun, S.J. Pleasure, et al. 2012. Regulation of prelamin A but not lamin C by miR-9, a brain-specific microRNA. *Proc. Natl. Acad. Sci. USA.* 109:E423–E431. https://doi.org/10.1073/pnas.1111780109

Kalwarczyk, T., N. Ziebacz, A. Bielejewska, E. Zaboklicka, K. Koynov, J. Szymański, A. Wilk, A. Patkowski, J. Gapiński, H.-J. Butt, and R. Hołyst. 2011. Comparative analysis of viscosity of complex liquids and cytoplasm of mammalian cells at the nanoscale. *Nano Lett.* 11:2157–2163. https://doi.org/10.1021/nl2008218

Kierfeld, J., P. Gutjahr, T. Kühne, P. Kraikivski, and R. Lipowsky. 2006. Buckling, bundling, and pattern formation: from semi-flexible polymers to assemblies of interacting filaments. *J. Comput. Theor. Nanosci.* 3: 898–911. https://doi.org/10.1166/jctn.2006.3078

Kimmel, C.B., W.W. Ballard, S.R. Kimmel, B. Ullmann, and T.F. Schilling. 1995. Stages of embryonic development of the zebrafish. *Dev. Dyn.* 203: 253–310. https://doi.org/10.1002/aja.1002030302

Kosodo, Y., T. Suetsugu, M. Suda, Y. Mimori-Kiyosue, K. Toida, S.A. Baba, A. Kimura, and F. Matsuzaki. 2011. Regulation of interkinetic nuclear migration by cell cycle-coupled active and passive mechanisms in the developing brain. *EMBO J.* 30:1690–1704. https://doi.org/10.1038/emboj.2011.81

Kwan, K.M., E. Fujimoto, C. Grabher, B.D. Mangum, M.E. Hardy, D.S. Campbell, J.M. Parant, H.J. Yost, J.P. Kanki, and C.B. Chien. 2007. The Tol2kit: a multisite gateway-based construction kit for Tol2 transposon transgenesis constructs. *Dev. Dyn.* 236:3088–3099. https://doi.org/10.1002/dvdy.21343

Lee, H.O., and C. Norden. 2013. Mechanisms controlling arrangements and movements of nuclei in pseudostratified epithelia. *Trends Cell Biol.* 23: 141–150. https://doi.org/10.1016/j.tcb.2012.11.001

Leung, L., A.V. Klopper, S.W. Grill, W.A. Harris, and C. Norden. 2011. Apical migration of nuclei during G2 is a prerequisite for all nuclear motion in zebrafish neuroepithelia. *Development.* 138:5003–5013. https://doi.org/10.1242/dev.071522

Levy, J.R., and E.L. Holzbaur. 2008. Dynein drives nuclear rotation during forward progression of motile fibroblasts. *J. Cell Sci.* 121:3187–3195. https://doi.org/10.1242/jcs.033878

Li, H., F. Guo, B. Rubinstein, and R. Li. 2008. Actin-driven chromosomal motility leads to symmetry breaking in mammalian meiotic oocytes. *Nat. Cell Biol.* 10:1301–1308. https://doi.org/10.1038/ncb1788

Luxton, G.W.G., E.R. Gomes, E.S. Folker, E. Vintinner, and G.G. Gundersen. 2010. Linear arrays of nuclear envelope proteins harness retrograde actin flow for nuclear movement. *Science.* 329:956–959. https://doi.org/10.1126/science.1189072

Marlow, F., J. Topczewski, D. Sepich, and L. Solnica-Krezel. 2002. Zebrafish Rho kinase 2 acts downstream of Wnt11 to mediate cell polarity and effective convergence and extension movements. *Curr. Biol.* 12:876–884. https://doi.org/10.1016/S0960-9822(02)00864-3

Matejčić, M., G. Salbreux, and C. Norden. 2018. A non-cell-autonomous actin redistribution enables isotropic retinal growth. *PLoS Biol.* 16:e2006018. https://doi.org/10.1371/journal.pbio.2006018

Mayer, M., M. Depken, J.S. Bois, F. Jülicher, and S.W. Grill. 2010. Anisotropies in cortical tension reveal the physical basis of polarizing cortical flows. *Nature.* 467:617–621. https://doi.org/10.1038/nature09376

Meyer, E.J., A. Ikmi, and M.C. Gibson. 2011. Interkinetic nuclear migration is a broadly conserved feature of cell division in pseudostratified epithelia. *Curr. Biol.* 21:485–491. https://doi.org/10.1016/j.cub.2011.02.002

Munro, E., J. Nance, and J.R. Priess. 2004. Cortical flows powered by asymmetrical contraction transport PAR proteins to establish and maintain anterior-posterior polarity in the early *C. elegans* embryo. *Dev. Cell.* 7: 413–424. https://doi.org/10.1016/j.devcel.2004.08.001

Nicolás-Pérez, M., F. Kuchling, J. Letelier, R. Polvillo, J. Wittbrodt, and J.R. Martínez-Morales. 2016. Analysis of cellular behavior and cytoskeletal dynamics reveal a constriction mechanism driving optic cup morphogenesis. *eLife.* 5:e15797. https://doi.org/10.7554/eLife.15797

Norden, C. 2017. Pseudostratified epithelia - cell biology, diversity and roles in organ formation at a glance. *J. Cell Sci.* 130:1859–1863. https://doi.org/10.1242/jcs.192997

Norden, C., S. Young, B.A. Link, and W.A. Harris. 2009. Actomyosin is the main driver of interkinetic nuclear migration in the retina. *Cell.* 138: 1195–1208. https://doi.org/10.1016/j.cell.2009.06.032

Oates, A.C., and R.K. Ho. 2002. Hairy/E(spl)-related (Her) genes are central components of the segmentation oscillator and display redundancy with the Delta/Notch signaling pathway in the formation of anterior segmental boundaries in the zebrafish. *Development.* 129:2929–2946.

Petrie, R.J., H. Koo, and K.M. Yamada. 2014. Generation of compartmentalized pressure by a nuclear piston governs cell motility in a 3D matrix. *Science.* 345:1062–1065. https://doi.org/10.1126/science.1256965

Phng, L.-K., V. Gebala, K. Bentley, A. Philippides, A. Wacker, T. Mathivet, L. Sauteur, F. Stanchi, H.-G. Belting, M. Affolter, and H. Gerhardt. 2015. Formin-mediated actin polymerization at endothelial junctions is required for vessel lumen formation and stabilization. *Dev. Cell.* 32: 123–132. https://doi.org/10.1016/j.devcel.2014.11.017

Pollard, S.M., M.J. Parsons, M. Kamei, R.N. Kettleborough, K.A. Thomas, V.N. Pham, M.K. Bae, A. Scott, B.M. Weinstein, and D.L. Stemple. 2006. Essential and overlapping roles for laminin alpha chains in notochord and blood vessel formation. *Dev. Biol.* 289:64–76. https://doi.org/10.1016/j.ydbio.2005.10.006

Reinsch, S., and P. Gönczy. 1998. Mechanisms of nuclear positioning. *J. Cell Sci.* 111:2283–2295.

Reymann, A.C., J.L. Martiel, T. Cambier, L. Blanchoin, R. Boujemaa-Paterski, and M. Théry. 2010. Nucleation geometry governs ordered actin networks structures. *Nat. Mater.* 9:827–832. https://doi.org/10.1038/nmat2855

Reymann, A.C., R. Boujemaa-Paterski, J.L. Martiel, C. Guérin, W. Cao, H.F. Chin, E.M. De La Cruz, M. Théry, and L. Blanchoin. 2012. Actin network architecture can determine myosin motor activity. *Science.* 336: 1310–1314. https://doi.org/10.1126/science.1221708

Robu, M.E., J.D. Larson, A. Nasevicius, S. Beiraghi, C. Brenner, S.A. Farber, and S.C. Ekker. 2007. p53 activation by knockdown technologies. *PLoS Genet.* 3:e78. https://doi.org/10.1371/journal.pgen.0030078

Roman, W., and E.R. Gomes. 2018. Nuclear positioning in skeletal muscle. *Semin. Cell Dev. Biol.* 82:51–56. https://doi.org/10.1016/j.semcdb.2017.11.005

Rowat, A.C., D.E. Jaalouk, M. Zwerger, W.L. Ung, I.A. Eydelnant, D.E. Olins, A.L. Olins, H. Herrmann, D.A. Weitz, and J. Lammerding. 2013. Nuclear envelope composition determines the ability of neutrophil-type cells to passage through micron-scale constrictions. *J. Biol. Chem.* 288: 8610–8618. https://doi.org/10.1074/jbc.M112.441535

Sauer, F.C. 1935. Mitosis in the neural tube. *J. Comp. Neurol.* 62:377–405. https://doi.org/10.1002/cne.900620207

Schindelin, J., I. Arganda-Carreras, E. Frise, V. Kaynig, M. Longair, T. Pietzsch, S. Preibisch, C. Rueden, S. Saalfeld, B. Schmid, et al. 2012. Fiji: an open-source platform for biological-image analysis. *Nat. Methods.* 9: 676–682. https://doi.org/10.1038/nmeth.2019

Shu, T., R. Ayala, M.D. Nguyen, Z. Xie, J.G. Gleeson, and L.H. Tsai. 2004. Ndel1 operates in a common pathway with LIS1 and cytoplasmic dynein to regulate cortical neuronal positioning. *Neuron.* 44:263–277. https://doi.org/10.1016/j.neuron.2004.09.030

Sidhaye, J., and C. Norden. 2017. Concerted action of neuroepithelial basal shrinkage and active epithelial migration ensures efficient optic cup morphogenesis. *eLife.* 6:e22689. https://doi.org/10.7554/eLife.22689

Soo, F.S., and J.A. Theriot. 2005. Large-scale quantitative analysis of sources of variation in the actin polymerization-based movement of *Listeria monocytogenes*. *Biophys. J.* 89:703–723. https://doi.org/10.1529/biophysj.104.051219

Spitzer, M., J. Wildenhain, J. Rappsilber, and M. Tyers. 2014. BoxPlotR: a web tool for generation of box plots. *Nat. Methods.* 11:121–122. https://doi.org/10.1038/nmeth.2811

Steigemann, P., C. Wurzenberger, M.H. Schmitz, M. Held, J. Guizetti, S. Maar, and D.W. Gerlich. 2009. Aurora B-mediated abscission checkpoint protects against tetraploidization. *Cell.* 136:473–484. https://doi.org/10.1016/j.cell.2008.12.020

Strzyz, P.J., H.O. Lee, J. Sidhaye, I.P. Weber, L.C. Leung, and C. Norden. 2015. Interkinetic nuclear migration is centrosome independent and ensures apical cell division to maintain tissue integrity. *Dev. Cell.* 32:203–219. https://doi.org/10.1016/j.devcel.2014.12.001

Strzyz, P.J., M. Matejcic, and C. Norden. 2016. Heterogeneity, cell biology and tissue mechanics of pseudostratified epithelia: coordination of cell divisions and growth in tightly packed tissues. *Int. Rev. Cell Mol. Biol.* 325: 89–118. https://doi.org/10.1016/bs.ircmb.2016.02.004

Swift, J., I.L. Ivanovska, A. Buxboim, T. Harada, P.C. Dingal, J. Pinter, J.D. Pajerowski, K.R. Spinler, J.W. Shin, M. Tewari, et al. 2013. Nuclear

lamin-A scales with tissue stiffness and enhances matrix-directed differentiation. *Science.* 341:1240104. https://doi.org/10.1126/science.1240104

Thisse, C., B. Thisse, T.F. Schilling, and J.H. Postlethwait. 1993. Structure of the zebrafish snaill gene and its expression in wild-type, spadetail and no tail mutant embryos. *Development.* 119:1203–1215.

Totsukawa, G., Y. Yamakita, S. Yamashiro, D.J. Hartshorne, Y. Sasaki, and F. Matsumura. 2000. Distinct roles of ROCK (Rho-kinase) and MLCK in spatial regulation of MLC phosphorylation for assembly of stress fibers and focal adhesions in 3T3 fibroblasts. *J. Cell Biol.* 150:797–806. https://doi.org/10.1083/jcb.150.4.797

Tran, P.T., L. Marsh, V. Doye, S. Inoué, and F. Chang. 2001. A mechanism for nuclear positioning in fission yeast based on microtubule pushing. *J. Cell Biol.* 153:397–411. https://doi.org/10.1083/jcb.153.2.397

Tsai, L.H., and J.G. Gleeson. 2005. Nucleokinesis in neuronal migration. *Neuron.* 46:383–388. https://doi.org/10.1016/j.neuron.2005.04.013

Tsai, J.W., K.H. Bremner, and R.B. Vallee. 2007. Dual subcellular roles for LIS1 and dynein in radial neuronal migration in live brain tissue. *Nat. Neurosci.* 10:970–979. https://doi.org/10.1038/nn1934

Tsai, J.W., W.N. Lian, S. Kemal, A.R. Kriegstein, and R.B. Vallee. 2010. Kinesin 3 and cytoplasmic dynein mediate interkinetic nuclear migration in neural stem cells. *Nat. Neurosci.* 13:1463–1471. https://doi.org/10.1038/nn.2665

Villefranc, J.A., J. Amigo, and N.D. Lawson. 2007. Gateway compatible vectors for analysis of gene function in the zebrafish. *Dev. Dyn.* 236:3077–3087. https://doi.org/10.1002/dvdy.21354

Wu, J., I.A. Kent, N. Shekhar, T.J. Chancellor, A. Mendonca, R.B. Dickinson, and T.P. Lele. 2014. Actomyosin pulls to advance the nucleus in a migrating tissue cell. *Biophys. J.* 106:7–15. https://doi.org/10.1016/j.bpj.2013.11.4489

Yi, K., B. Rubinstein, J.R. Unruh, F. Guo, B.D. Slaughter, and R. Li. 2013. Sequential actin-based pushing forces drive meiosis I chromosome migration and symmetry breaking in oocytes. *J. Cell Biol.* 200:567–576. https://doi.org/10.1083/jcb.201211068